Ramy Al-Zubeidi

Analytical loss calculation models of a choke-based filter

School of Technology and Innovations
Master's thesis in Electrical Engineering
Energy and Information Technology, M.Sc. (Tech.)

Vaasa 2024

UNIVERSITY OF VAASA
School of Technology and Innovations
Author: Ramy Al-Zubeidi
Title of the Thesis: Analytical loss calculation models of a choke-based filter
Degree: Master of Science in Technology
Discipline: Electrical Engineering
Supervisor: Kimmo Kauhaniemi
Instructor: Timo Kantola
Evaluator: Timo Vekara
Year: 2024 **Pages:** 91

ABSTRACT:

The purpose of this thesis is to examine the loss calculation of the foil winding choke and to develop an analytical calculation model to support the design of the main circuit. The analytical calculation model should be easy to use, accurate, reliable and flexible. The analytical calculation model should calculate the winding and core losses of the choke. The tool must be able to determine the choke losses at different load points when the output frequency and modulation index vary.

Two analytical calculation models were developed to support the main circuit design. The operation of the calculation models is based on the baseline values entered by the user, which are used in the calculation models to determine the winding and core losses that are important to the choke. The first analytical calculation model calculates only core and winding losses. In addition to this, a separate analytical calculation model to determine AC winding losses was developed to support FEMM-2D simulation software. The purpose of the simulation model is to supplement the calculation tool to determine the exact loss result.

During this thesis, some simulations and calculations were performed. The core simulations were used to investigate, among other things, the effect of the air gap. Primarily, it was examined how the fringing flux behaves when the number and length of air gaps increase. Winding simulations were performed to study, among other things, winding losses. In addition to this, the winding at the air gaps was examined, as well as the effect of the core shape on the magnitude of the flux density and total losses. Simulations and calculations were also performed to obtain more information about skin and proximity effects.

As a result of the work, the necessary analytical calculation models were developed in the MATLAB environment. Regarding DC winding losses, the relative error between the analytical calculation model and the simulation result was 13 %, which indicates that the results corresponded well to each other. Similarly, for AC winding losses, the relative error between the analytical calculation model and the simulation result was 27 %. This difference can be explained by the incomplete calculation of winding resistance in a simulation environment since the exact calculation of the winding resistance can only be done using the defined equations. Core losses were modeled using Steinmetz equation. According to the analytical calculation model, maximum losses in the frequency range from 50 Hz to 20 kHz occur at 4 kHz.

KEYWORDS: LCL filter, foil winding, choke, core loss, winding loss, skin effect, proximity effect, Steinmetz

VAASAN YLIOPISTO
Tekniikan ja innovaatiojohtamisen yksikkö
Tekijä: Ramy Al-Zubeidi
Tutkielman nimi: Kuristinpohjaisen suodattimen analyyttiset häviölaskentamallit
Tutkinto: Diplomi-insinööri
Oppiaine: Sähkötekniikka
Työn valvoja: Kimmo Kauhaniemi
Työn ohjaaja: Timo Kantola
Työn tarkastaja: Timo Vekara
Valmistumisvuosi: 2024 **Sivumäärä:** 91

TIIVISTELMÄ:

Tämän lopputyön tarkoituksena on tarkastella foliokäämisen kuristimen häviölaskentaa ja kehittää pääpiirin suunnittelun tueksi analyyttinen laskentamalli. Analyyttisen laskentamallin tulee olla helppokäyttöinen, tarkka, luotettava ja joustava. Analyyttisestä laskentamallista tulee selvitä kuristimen käämitys- ja rautaydinhäviöt. Työkalun tulee pystyä määrittämään kuristinhäviöt eri kuormituspisteissä, kun lähtötaajuus ja modulaatioindeksi vaihtelevat.

Pääpiirin suunnittelun tueksi kehitettiin kaksi analyyttistä laskentamallia. Laskentamallien toiminta perustuu käyttäjän syöttämiin lähtöarvoihin, joiden perusteella laskentamallit määrittävät kuristimelle tärkeimmät käämi- ja sydänhäviöt. Ensimmäinen analyyttinen laskentamalli laskee kuristimen rautasydämen ja käämityksen häviöt. Tämän lisäksi FEMM-2D -simulointiohjelmiston tueksi kehitettiin erillinen analyyttinen laskentamalli AC-käämityshäviöiden määrittämiseksi. Simulointimallin tarkoituksena on täydentää laskentatyökalua tarkan häviötuloksen määrittämiseksi.

Työn aikana suoritettiin joitakin simulointeja ja mittauksia. Rautaytimelle tehtyjen simulointien avulla haluttiin selvittää muun muassa ilmaraon vaikutusta. Lähtökohtaisesti selvitettiin, miten hajavuo käyttäytyy, kun ilma-aukkojen määrä ja pituus kasvavat. Käämitykselle tehtyjen simulointien avulla selvitettiin muun muassa muodostuneet käämihäviöt. Tämän lisäksi selvitettiin käämitystä ilma-aukkojen kohdalla ja sydämen muodon vaikutusta vuontiheyden suuruuteen ja kokonaishäviöihin. Simulointien ja mittausten avulla haluttiin saada myös lisätietoa virranahtoja lähivaikutusilmiöistä.

Työn tuloksena saatiin kehitettyä tarvittavat analyyttiset laskentamallit, jotka molemmat luotiin MATLAB-ympäristöön. DC-käämityshäviöiden osalta analyyttisen laskentamallin ja simulointituloksen virhemarginaali oli 13 %, mikä osoittaa, että tulokset vastasivat hyvin toisiaan. Vastaavasti AC-käämityshäviöiden osalta analyyttisen laskentamallin ja simulointituloksen virhemarginaali oli 27 %. Tätä eroa voidaan selittää simuloinnin puutteellisella laskennalla, koska käämiresistanssin tarkka laskenta onnistuu vain määriteltyjen yhtälöiden avulla. Sydänhäviöt mallinnettiin Steinmetzin yhtälön avulla. Analyyttisen laskentamallin mukaan suurimmat häviöt taajuusalueella 50 Hz – 20 kHz syntyvät 4 kHz kohdalla.

AVAINSANAT: LCL-suodatin, foliokäämi, kuristin, sydänhäviöt, käämihäviöt, virranahto, lähivaikutus, Steinmetz

Contents

1 Introduction 15

2 Grid converter with an LCL filter 18

2.1 Four connection methods of the 3-phase connection system 18

2.2 Grid-converter modeling 22

2.2.1 LCL filter 26

2.2.2 Dynamic behavior of L, LC and LCL circuits: bode diagram 30

3 Choke winding 34

3.1 Polarity of coils 34

3.2 Foil conductor 35

3.2.1 Skin and proximity effects 35

3.2.2 Calculation of ohmic losses 37

3.2.3 Winding resistance 39

3.2.4 Determination of inductance 40

3.2.5 Temperature dependency of resistivity 43

4 Choke core 44

4.1 The analogy between magnetic and electric circuit 44

4.2 Core assembled from cut sheets to minimize eddy current losses 46

4.3 Temperature dependency of resistivity 49

4.4 Definition of saturation magnetic flux density 50

4.5 Typical model for calculating core losses 53

5 Results and evaluation 55

5.1 Choke modeling using simulation software 55

5.2 Design of analytical loss calculation models 58

5.2.1 Analytical loss calculation model for calculating AC winding and core losses 59

5.2.2 Analytical loss calculation model for calculating AC winding losses using simulation software 67

5.3 The results of calculation models and their comparison 71

5.3.1 AC winding and core losses of the analytical calculation model 71

5.3.2 AC and DC winding losses of the analytical calculation model and their comparison with the simulation result 73

6 Conclusion 76

References 79

Appendices 88

Appendix 1. Analytical calculation model for core and winding losses 88

Appendix 2. Analytical calculation model for AC winding losses 90

Figures

Figure 1. Low voltage network, TN-C power distribution system. 19

Figure 2. Four different types for 3-phase connection. The figure shows Y-Y connection (a), Y-Δ connection (b), Δ-Δ connection (c) and Δ-Y connection (d). 20

Figure 3. Symmetrical Y-Δ circuit (a). Phase angle difference between line and phase voltage (b). 21

Figure 4. Multidrive modules with direct liquid cooling (ABB, n.d). 23

Figure 5. Grid-connected three-phase converter with DC load (a). Grid-connected three-phase converter with AC motor (b). 25

Figure 6. Current behavior in an inductor that normally opposes a change in current. The voltage across the inductor when the current is constant (a). The voltage across the inductor, as the current changes (b). 27

Figure 7. The ripple simulation current of the converter is compared to the fundamental current (a) (Rahman, 2016, p. 9). The *BH* curve illustrates the loss energy of a large loop, which originates from the fundamental waveform, and correspondingly, the loss energy of small loops originates from the high-frequency ripples (b) (Muhlethaler, 2012, p. 4). 29

Figure 8. Bode diagram of L circuit. 31

Figure 9. Bode diagram of LC circuit. 32

Figure 10. Bode diagram of LCL circuit. 32

Figure 11. Polarity of windings. Inside the current winding, the direction of the flux it causes (a). If current, i_1 is applied to the winding, it causes a flux in the winding with the direction shown in Figure (b). The induced flux flows upward through this winding and downward through the other windings (c) and (d). 35

Figure 12. Current density and magnetic field in foil conductor. According to right-hand rule, the thumb indicates toward the current density, J_x, which is

in same direction as unit vector e_x, while the other fingers indicate toward the magnetic field strength, *H* (Biela, 2012, p. 29). 36

Figure 13. A cross-section of a foil conductor parallel to the unit vector ex. The amplitude of the *H*-field, H_s acts in the direction of the unit vector e_z (Biela, 2012, p. 34). 36

Figure 14. Illustration of a magnetic flux density, $\boldsymbol{B}$ generated by a current *I*. 41

Figure 15. Typical choke core model consisting of a foil winding, a core and an air gap (a). The electrical equivalent circuit of the entire core magnetic circuit (b). 46

Figure 16. A core of the choke used in this thesis shown from the front and side (a) and (b). Insulation (lamination) between cut sheets is required to reduce eddy currents (c) (Mclyman, 2004, p. 108). 48

Figure 17. Illustration of the current waveform with ripple. The load current versus time is examined at (a) and the magnetic flux density versus time at (b). 51

Figure 18. A core with an induced magnetic flux due to an AC current of 652 A on the left-hand of the limb and a frequency of 50 Hz. 56

Figure 19. Magnetic flux density distribution of choke-based core saturated with 652 A AC current at a frequency of 50 Hz. 57

Figure 20. The magnetic flux density, $\boldsymbol{B}$ is highest in the air gaps and extends to the winding area, causing eddy currents and additional losses in the windings. 58

Figure 21. Definition of variables such as frequency and effective current. 60

Figure 22. The equation required to calculate the winding turns and the effective cross-sectional area of the core. 61

Figure 23. Amplitude of AC component of magnetic flux density. 62

Figure 24. Determination of conductor resistivity. 63

Figure 25. The equation used to determine the volume of a winding conductor. 63

Figure 26. Determination of DC winding resistance. 64

Figure 27. Determination of AC winding resistance. 64

Figure 28. Determination of the temperature dependence of the core from the final temperature. 65
Figure 29. Determination of core losses by using the Steinmetz equation. 66
Figure 30. Determination of AC winding losses in six different frequency ranges. 67
Figure 31. Simulated winding losses of the choke prototype. 68
Figure 32. Definition of winding losses in 2D and 3D environment. 70
Figure 33. Core losses in 6 frequency ranges from 50 Hz to 18.2 kHz. Choke core losses were determined using an analytical loss calculation tool. 72
Figure 34. Winding losses in 6 frequency ranges from 50 Hz to 18.2 kHz. The AC winding losses of the choke-based filter were determined using an analytical loss calculation tool. 73
Figure 35. Columns illustrate the losses of an AC winding, where columns 1 to 3 are the loss calculation results of a 2D-3D environment (Appendix 2) and column 4 is the calculation result of a numerical method (Appendix 1). The relative error between the calculated losses and the simulation result is illustrated by the orange curve. 74
Figure 36. Columns illustrate DC winding losses, where columns 1-3 are the results of a 2D-3D environment loss calculation (Appendix 2). The margin of error between the calculated losses and the simulation result is illustrated by the orange curve. 75
Figure 37. Analytical loss calculation model of the choke-based filter for calculating core and AC winding losses. 89
Figure 38. Analytical loss calculation model of the choke-based filter for calculating AC winding losses. The calculation model uses the FEMM 2D simulation software. 91

Tables

Table 1. Resistance and conductivity specified for conductors at 20 °C (Kazimierczuk, 2014, p. 165). 43

Table 2. The material parameters of the choke prototype examined in this thesis. 50

Symbols and abbreviations

Greek symbols

α	Attenuation constant
α_{d}	Dowells attenuation constant (Dowell material coefficient)
β	Phase constant
δ	Skin depth
η	Dowells porosity factor
μ	Permeability
μ_{r}	Relative permeability of the material
μ_0	Permeability of the free space
ρ	Electrical resistivity (also called specific electrical resistance)
ρ_{T0}	Resistivity at temperature T_0 (initial temperature)
ρ_{T}	Resistivity at temperature T (final temperature)
φ	Phase angle
Φ	Magnetic flux
Φ_{core}	Magnetic flux in core
ω	Angular frequency

Other symbols

A	Cross-sectional area
A_{gap}	Cross-sectional area of the air gap
A_{core}	Cross-sectional area of the core
$A_{\mathrm{core(eff)}}$	Effective cross-sectional area of the core
A_{foil}	Cross-sectional area of a foil conductor

A_L	Inductance per turn
A_{round}	Cross-sectional area of a round conductor
b_{Fe}	Breadth of cut sheet (laminated pack)
h_{Fe}	Length of laminated cut sheet pack
$\boldsymbol{B}$	Magnetic flux density
$\boldsymbol{B}_{peak}$	Peak magnetic flux density
$\boldsymbol{B}_{sat}$	Saturation magnetic flux density
$\Delta\boldsymbol{B}$	Peak value of AC component of magnetic flux density
$c_{core(T0)}$	Models the temperature dependency of the initial temperature, T_0
$c_{core(T)}$	Models the temperature dependency of the final temperature, T.
D	Real part of complex number
$\boldsymbol{E}$	Electric field strength
f	Frequency
$\boldsymbol{F}$	Magnetomotive force, *mmf*
Fe_{yoke}	Yoke breadth
Fe_{limb}	Limb height
h	Depth
$\boldsymbol{H}$	Magnetic field intensity
I	Current
i_{max}	The current amplitude at which the core becomes saturated. Here $i_{\max} = i_{\mathrm{sat}}$.
I_{peak}	Peak current
I_{rms}	Rated rms current
$\boldsymbol{J}$	Current density

l	Length
l_{core}	Magnetic path length
l_{w}	Length of winding wire
l_{gap}	Length of air gap
$k_{\text{H(DC)}}$	Material-dependent proportionality factor determined at a given temperature, T. Coefficient models the dependence of the losses on the $\boldsymbol{H}_{\text{DC}}$-field.
L	Inductance
M	Real parts of complex numbers
F_{R}	Ratio of AC value of $R_{\text{W(AC)}}$ to DC value
N	Number of winding turns
P_{w}	Winding power loss
P_{core}	Core loss
R	Resistance
R_{m}	Magnetic reluctance of core
R_{core}	Reluctance of core
R_{f}	Resistance correction factor
R_{f}	Resistance correction factor
R_{gap}	Reluctance of air gap
$R_{\text{w(AC)}}$	Winding AC resistance
$R_{\text{w(DC)}}$	Winding DC resistance
Sf_{Fe}	Core stacking factor
T	Final temperature
T_0	Initial temperature
U	Average voltage
U_{DC}	DC voltage

u_L	Inductor voltage
U_{LL}	Line-to-line voltage
W_a	Core window area
W_b	Breadth of winding
W_h	Height of winding
W_{mlt}	Winding mean length per turn
$W_{N/layers}$	Number of layers (number of whole layers in a winding portion)
Z	Impedance

Abbreviations

AC	Alternating current
ACU	Auxiliary control unit
DC	Direct current
DSU	DIode supply unit
ICU	In-coming unit
INU	Inverter unit
ISU	IGBT supply unit
LC	Liguid cooled
MMF	Magnetomotive force
MLT	Mean length per turn
PLL	Phase-locked loop
PWM	Pulse-width modulation
SC	Solar cell

TSU	Thyristor supply unit
Δ	Delta-configuration
Y	Y-configuration

1 Introduction

Grid converters will play an increasingly important role in industrial applications in the energy system of the future. Typically, the grid converter is used for example in fuel cells, photovoltaic systems and marine vessels. In general, a power electronics-based DC-AC power converter is used to connect the generated energy to the grid. However, a significant part of the electricity produced is consumed by various electric motors and machines.

Potential development measures for power electronics-based converters include energy efficiency, reliability and cost efficiency. Basically, the energy efficiency of the converter can be improved by reducing losses. This is partly achieved by minimizing current and voltage ripples, which increase the temperature of the converter and shorten the service life.

This thesis focuses on a choke-based converter and the design of an analytical loss calculation tool. Traditionally, the choke L is part of the LCL filter, which has been used to dampen harmonic currents generated by power electronic components. Current ripple is a significant loss factor for a choke. If the harmonic currents are not filtered, they can interfere with other power electronic equipment and the transformer in the grid. However, the choke alone (L filter) is not enough to filter sufficiently to meet the attenuation requirements at the highest frequencies (above 1 kHz). Thus, instead of one choke (L filter), two choke (LCL filter) have been used.

The core losses of the choke mostly consist of hysteresis and eddy current losses. Losses are mainly hysteresis losses, but at high frequencies (above 1 kHz) or high dimensional cores eddy current losses are also affected (Muhlethaler, 2012, p. 113–114; Biela, 2011, p. 15). Typically, eddy current losses can be reduced by making the core from thin layers insulated from each other. Correspondingly, a high-frequency current causes eddy currents inside the conductor, which also causes eddy currents in the conductors that are around the field. These phenomena are called skin effect and proximity effect, which

generate losses. Typically, winding losses have been reduced by using foil windings instead of round conductors.

The aim of this thesis is to design two analytical calculation tools to determine the losses of the choke. Calculation models must account for core and winding losses. The purpose of this thesis is to design analytical calculation tools that are as easy to use, accurate, reliable and as flexible as possible, so that they would be suitable for use as loss calculation tools for different types of choke prototypes. The tools should be easy to use in the sense that they are suitable for parameterization and variation as needed. The tools must be able to determine choke losses at different load points, as well as different values of the output frequency and modulation index. As part of the work, the accuracy of the calculation is verified through simulations and calculations. In this thesis, the calculations and simulations are examined for one choke prototype.

This thesis consists of six main chapters. Chapter 2 examines the basic principle of a grid-connected converter with an LCL filter. Section 2.1 examines the connection methods of the 3-phase system. Section 2.2 discusses liquid-cooled frequency converter in more detail. The structure of the converter is examined in the form of figures. In addition, the dynamic behavior of the L, LC and LCL circuit is examined as a function of frequency by using bode diagrams.

Chapter 3 discusses the winding of the choke and its loss calculation. Section 3.1 discusses the mutual polarity of the windings when there are several windings in the choke structure. Skin and proximity phenomena for the foil conductor are further discussed in Section 3.2. Loss calculation is also discussed without skin and proximity effects. In addition, the necessary equations for calculating winding losses are defined, as well as other useful equations. The derivation of the equations is presented so thoroughly that it is possible to modify them if necessary (for example by changing the operating temperature or the thermal resistance equation).

Chapter 4 discusses the iron core of the choke and its loss calculation. Section 4.1 analyses the analogy between the magnetic circuit of the choke and the electrical circuit. The sheet core is usually made by assembling the core from cut sheets, which is discussed in more detail in Section 4.2. To reduce eddy current losses, the sheets are insulated from each other. Section 4.3 examines the calculation of the temperature dependence of the core. Typically, the effect of core temperature must be considered if the core material changes, as the saturation flux density is strongly dependent on temperature. In power electronics, the dimensioning of the choke is usually based on the fact that it must withstand a certain current without becoming saturated and that losses must not cause excessive heating. The dimensioning method given in Section 4.4 is in accordance with this. The last Section 4.5 discusses the most typical Steinmetz loss calculation model for determining iron core losses.

Chapter 5 presents conclusions about the results of the work and evaluates their significance. In Section 5.1, simulation is made for the choke prototype using the FEMM 2D software. The core and winding of the choke prototype are examined from the simulation results. The software examines, among other things, the effect of the air gap and winding on the behavior of the fringing flux, as well as the resulting winding losses. Analytical calculation models for calculating core and winding losses are defined in Section 5.2. Basically, it is defined which equations of the theoretical part have been used in the calculation models. Section 5.3 discusses the calculation results and the conclusions of the calculation models in more detail. Finally, chapter 6 summarizes the main points of the thesis.

2 Grid converter with an LCL filter

Renewable energy sources include hydro, solar and wind energy, which are used to generate electricity, and which aim to transfer the electricity produced to the grid. The produced electricity is later transferred to the electricity grid. Electricity transfers take place by converting the frequency and current of the produced renewable energy to a form suitable for the electricity grid. Typically, the grids current is a sinusoidal AC current. A grid converter based on power electronics is responsible for the conversion process.

With stricter energy requirements, the use of the LCL filter increases its share in renewable energy systems such as solar inverters and wind turbine converters. Renewable energy systems have power semiconductors, such as IGBT-switches, which bring harmonics to the system. These harmonics increase the number of losses and electromagnetic interference and reduce current quality. The LCL filter is designed to efficiently suppress harmonic switching waves (voltages and currents) at the highest frequencies. Other advantages of LCL filter include better performance, cost efficiency, compact size and lower weight. The disadvantage of the LCL filter is its resonance frequencies, which can develop harmonics or directly affect the balance of the operating system. This chapter presents the theory related to the grid converter, system modeling, an overview of the LCL converter and choke. In addition to this, the sections examine in more detail the difference between L, LC and LCL filters, and finally the ripple current is discussed.

2.1 Four connection methods of the 3-phase connection system

Figure 1 is an illustration of a simple circuit diagram of a three-phase system, and specifically a 4-wire, 3-phase (TN-C) system. First, each phase has its own voltage source marked to simplify the illustration, when typically, the voltage comes from the same generator, in other words from one voltage source. Voltage sources configures as a Y-connection supply current and voltage to the load. The three windings of the generator are separated by a phase difference of 120 degrees. Thus, the phase difference of each

phase is 120 degrees. In other words, the phase shift of the first voltage source is 0 degrees, the second -120 degrees and the third -240 degrees. In each of the three phases, the current always flows from the voltage source to the load and provides a voltage with a phase difference of 120 degrees. If there is a balanced 3-phase system, the voltage should have the same magnitude and the impedance, Z of each conductor should be same. In addition to this, the sum of all currents should be 0.

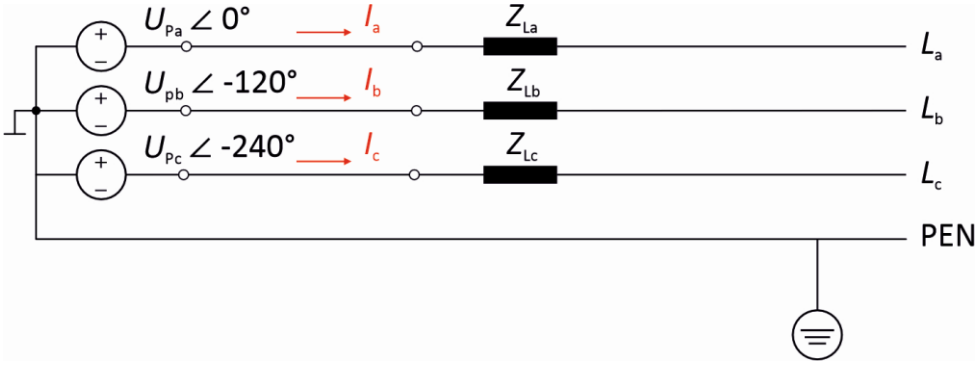

Figure 1. Low voltage network, TN-C power distribution system.

The source or load can be connected separately in two different ways, where Y-configuration or Δ (delta) configuration, as can be seen in Figure 2. There are four connection methods that can be used to connect a source or a load. Thus, the connection method can be Y-Y, where both sources and the load are connected according to the Y-connection method. The connection method can also be Y-Δ, where the sources are configured to the connection method Y and the load respectively, for connection method Δ. What can also be seen is Δ-Δ where both the load and the sources are configured as a delta connection. Finally, it is possible to come across a Δ-Y connection, where all sources are turned to a Δ-connection and the load is connected as a Y-connection. In general, the sources are usually configured as a Y-connection and the load, respectively, as a Δ-connection. What can be noticed is that no neutral conductor is used between the Y-Δ-connection and correspondingly a neutral conductor is used in the Y-Y connection.

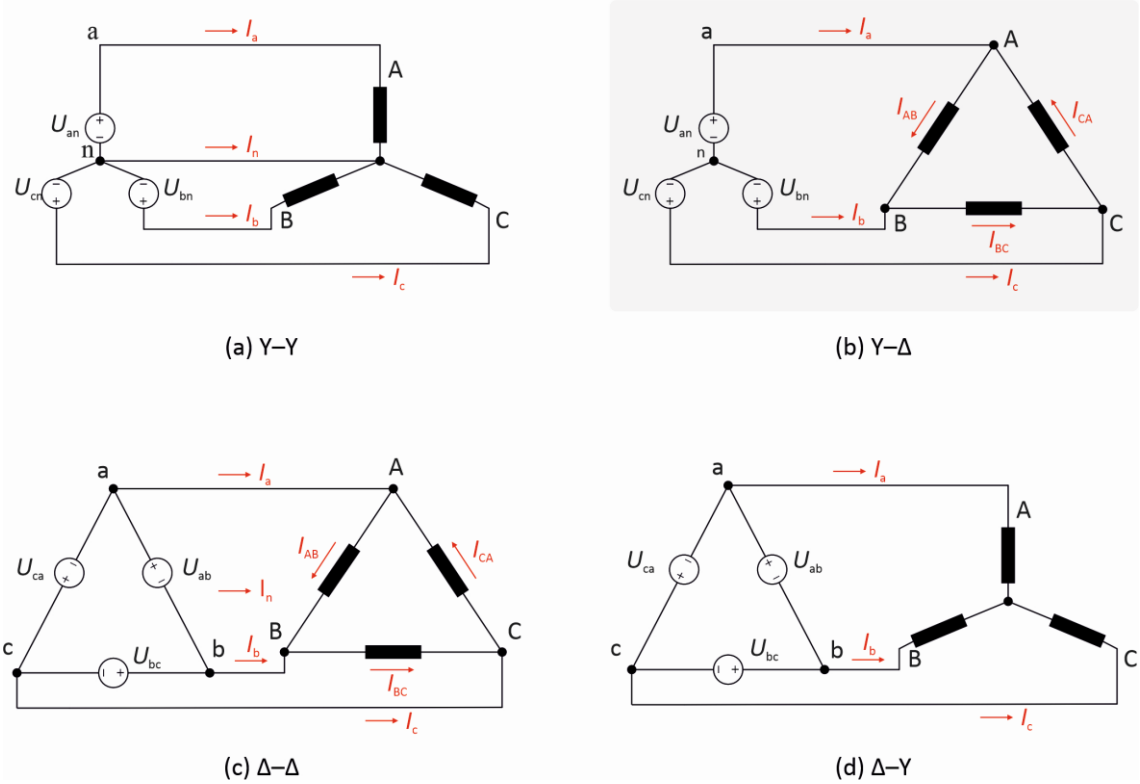

Figure 2. Four different types for 3-phase connection. The figure shows Y-Y connection (a), Y-Δ connection (b), Δ-Δ connection (c) and Δ-Y connection (d).

Initially, what is interesting is to find out the relationship between the phase and line currents (grid current) and the phase and line voltage of the Y-Δ circuit in Figure 3a. The wire currents all the way from the source to the load are I_a, I_b and I_c. The phase currents are the currents passing through the load capacitors from the point A to point B, B-C and C-A. The line voltage at the load from point A-B is the same line voltage at the source between a-b. The phase voltage at the source is a-n, b-c, and c-n.

Figure 3b shows a graphical representation illustrating the differences between line current and phase current, as well as the differences between line voltages and phase voltages. In addition, there are differences between line voltages and phase voltages. From Figure 3, part b, the line voltage has a greater magnitude than the phase voltage and the difference is $\sqrt{3}$. In addition, what can be noticed is that the line voltage leads the phase voltage by 30 degrees. When dealing with currents, what should be noted is that the line

current is greater than the phase current by a factor of $\sqrt{3}$. In addition, what should be remembered is that the line current lags the phase current by 30 degrees.

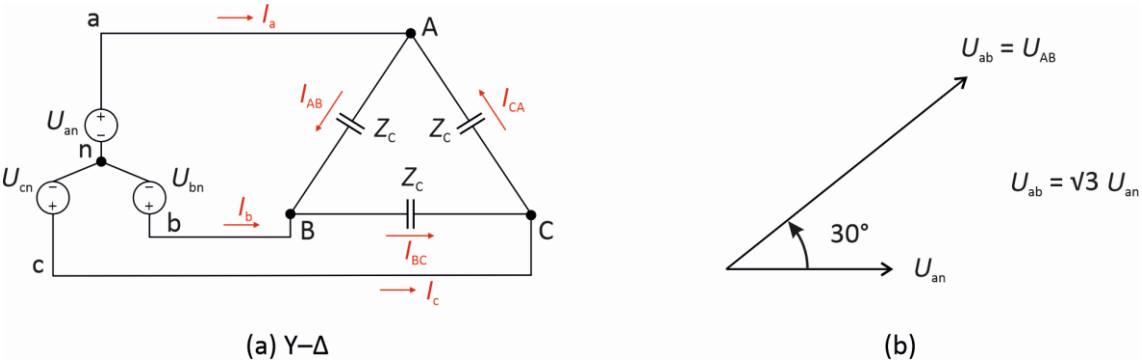

Figure 3. Symmetrical Y-Δ circuit (a). Phase angle difference between line and phase voltage (b).

Line (line-to-line) voltage, U_{LL} can be calculated from the equation

$$U_{\mathrm{LL}} = \sqrt{3}\, U_{\mathrm{p}} \angle\varphi - 30°\,, \tag{1}$$

where U_p is the phase voltage and the phase difference is 30 degrees. For example, the line voltage between a-b can be calculated as follows

$$U_{\mathrm{ab}} = \sqrt{3}\, U_{\mathrm{an}} \angle\varphi + 30°\,, \tag{2}$$

where U_{AB} is the voltage between a and n and with a phase angle of 30 degrees. The line currents are defined using the following equations

$$I_{\mathrm{L}} = \sqrt{3}\, I_{\mathrm{P}} \angle\varphi - 30° \tag{3}$$

and

$$I_{\mathrm{a}} = \sqrt{3}\, I_{\mathrm{AB}} \angle\varphi - 30°, \tag{4}$$

where I_P is the magnitude of the phase current with a phase angle difference of -30 (a lag of -30 degrees). The phase current, I_{AB} is defined using the following equation

$$I_{\mathrm{AB}} = \frac{U_{\mathrm{AB}}}{Z_{\mathrm{C}}} = \frac{U_{\mathrm{ab}}}{Z_{\mathrm{C}}}, \tag{5}$$

where U_{AB} is the line voltage A-B and Z_C is the load (capacitor) impedance.

2.2 Grid-converter modeling

A stable grid needs a grid converter to adjust the voltage, improve the power quality, support the frequency, and filter the signal. One important feature of the drive is that when the motor speed requirement in a particular application change, the drive can simply increase or decrease the motor speed to meet the grid requirements. In the grid converter, the output voltage and frequency can be controlled using pulse width modulation (PWM). Voltage regulators are needed to tune the voltage. Typically, the current and signal quality is improved through a filter. The grid converter ensures the stable operation of the grid in the smart electricity system of the future.

This thesis focuses on ABB's modular frequency converter product family. Before this master's thesis, a new liquid-cooled frequency converter cabinet was under development. With the new architecture, even more effort is put into the frequency converter's ease of use, modularity, energy saving and maximizing process efficiency. The purpose of utilizing liquid cooling was to reduce heat losses and reduce the need for air cooling.

Figure 4 shows the AC-based multidrive frequency converter cabinet, which consists of several separate units. The necessary modules are placed inside the units depending on the application and are later connected. The supply unit includes Auxiliary control unit (ACU), in-coming unit (ICU) and diode supply unit (DSU)/ thyristor supply unit (TSU)/ IGBT supply unit (ISU). The number of inverter units (INU) changes according to the

customer's requirements. Depending on the application, the supply unit has either a diode bridge, a thyristor bridge, or an IGBT bridge. The LCL filter module only comes with the IGBT supply unit.

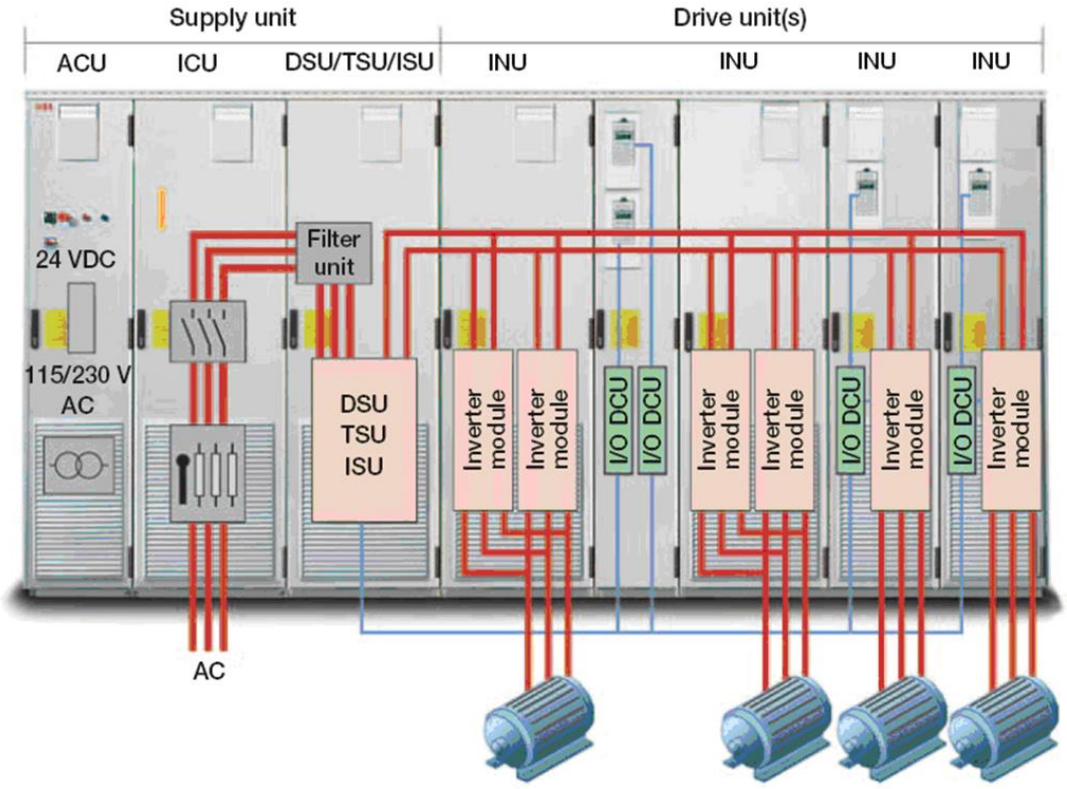

Figure 4. Multidrive modules with direct liquid cooling (ABB, n.d).

Figure 5a illustrates the topology of the grid-converter and the LCL filter. The system consists of six parts, with DC power source, inverter, intermediate voltage circuit, LCL filter and grid. The inverter unit (INU) converts the incoming direct current, DC into alternating current, AC. The purpose of the intermediate voltage circuit, U_{DC} is to filter out impurities in the DC voltage and to try to keep the voltage as constant as possible, as well as to act as an energy storage.

The pair of power semiconductor switches (IGBT and with diode) of each phase of the inverter (IGBT supply unit), which are used to transfer the necessary power, are connected to the choke coils, L_2. In other words, the power is transferred from the ISU

module (DC to AC) as pulse modulated (PMW) to phases a, b, c, where the voltage is adjusted by changing the pulse ratio (Haanpää, 2016, p. 14). The signal controls the IGBT switches so that the phase conductor is alternately connected to the DC intermediate circuit, U_{DC} + and - poles. Each phase of the inverter is connected to a damped L/ C filter. The semiconductor switches of the inverter (ISU, IGBT supply unit/ AFE, active front end), which are 6 pieces in total, are used to connect the phase conductors and are connected to the intermediate voltage circuit, U_{DC}. Semiconductors switches have a parallel-connected diode, which allows reactive current to be involved between the inverter and the grid. The power is transferred from the intermediate voltage circuit with the help of an inverter to the grid in AC or, correspondingly, from the grid to the intermediate voltage circuit in DC. The output current $i_{2,\mathrm{a}}$ of the inverter contains unwanted high-frequency harmonic currents caused by the PWM, which the LCL filter must tolerate.

The filter in Figure 5a consists of two separate chokes, with chokes on the grid and converter side, and a capacitor. The choke (L_2) tends to suppress the sinusoidal basic current (grids current). Similarly, the LCL filter attenuates the sinusoidal basic current and at the same time reduces the harmonic currents generated by the switch functions in the converter. The capacitor reduces the power factor of the filter, but at the same time the capacitor cannot be increased excessively as this would lead to an increase in reactive power, which in turn reduces the power factor of the filter.

The converter application illustrated in Figure 5b is considered in this thesis. The converter in Figure 5b is almost identical to the frequency converter in Figure 4, and the only difference is the location of the filter module, which is placed at the motor side in Figure 5. In addition, depending on the application, a diesel generator serves as the power source of the frequency converter in the marine industry. It is assumed here that there is a filter module on the grid side that filters the interference currents generated by the power electronics components. The incoming alternating current is rectified through the rectifier module (ISU) and converted into an AC current suitable for the AC motor with

the help of the inverter module (INU). Additional interference currents are filtered by a filter module located on the motor side.

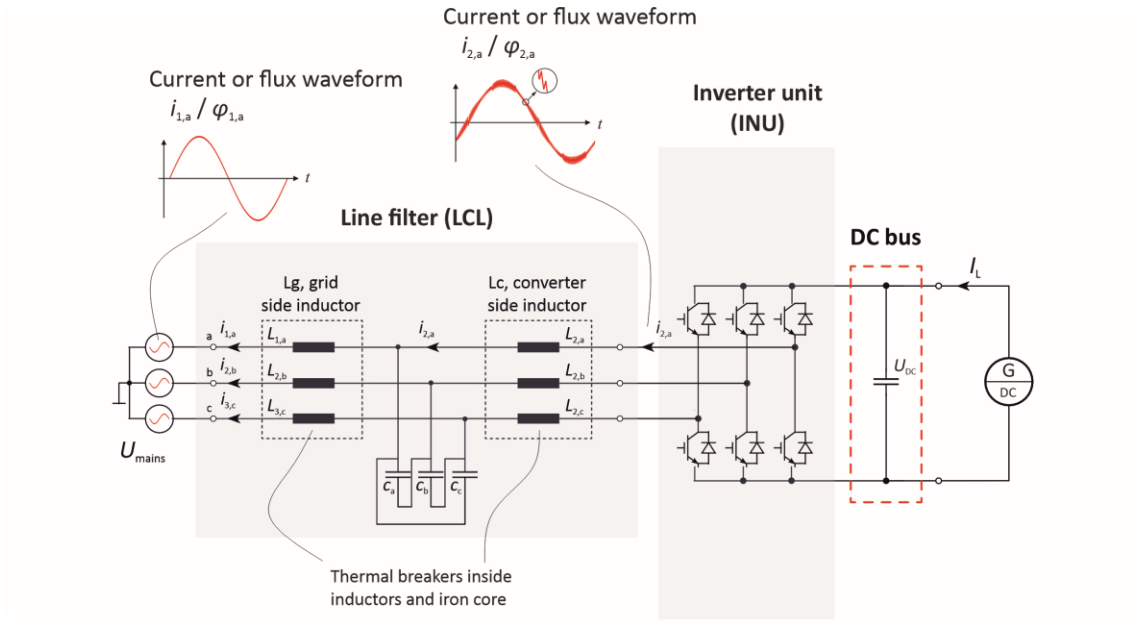

(a)

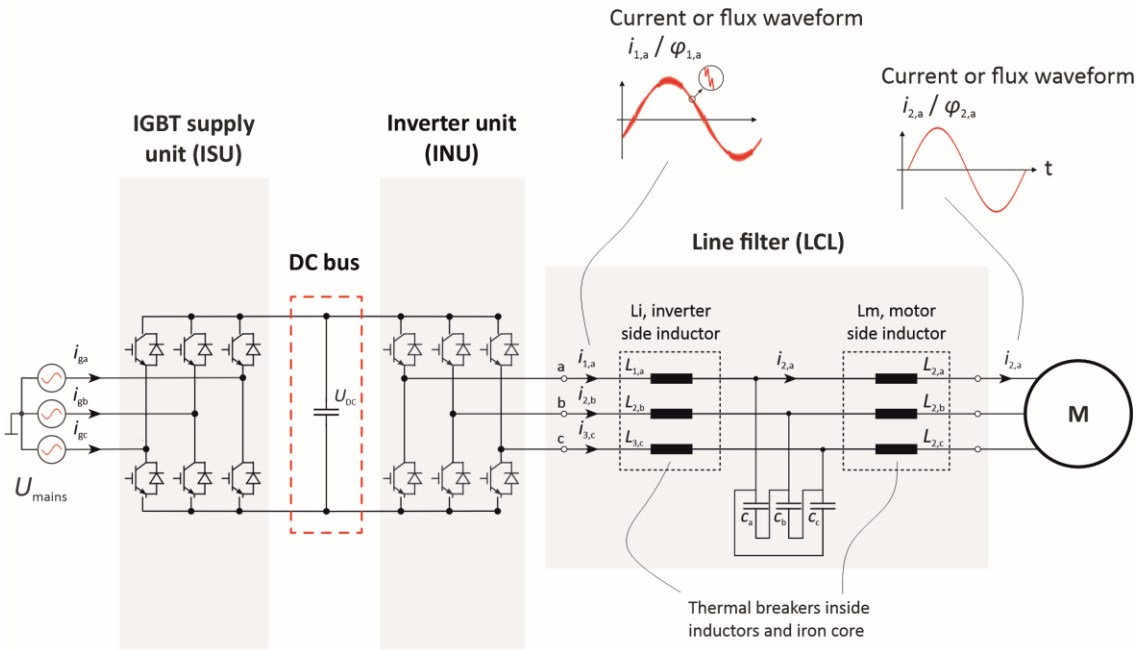

(b)

Figure 5. Grid-connected three-phase converter with DC load (a). Grid-connected three-phase converter with AC motor (b).

2.2.1 LCL filter

Power electronic devices such as frequency converters or inverters create harmonics and other unwanted effects on the electrical grid. Depending on the application, the models can be equipped with a filter module, which reduces high-frequency emissions. Power electronics based LCL filters are especially important in systems with non-linear loads. The LCL filter helps to reduce harmonic distortion, improve the quality of electricity, and meet standards.

It turns out that the L filter is a choke consisting of a core and a winding. Typically, the choke core material is a magnetically conductive material, such as a ferromagnet or ferrite. Correspondingly, copper or aluminum conductors are used in the winding. Normally, the choke used in power electronic applications can be one, two or three-phased. In this thesis, the focus is on three-phase chokes.

The choke has a very special property, the choke resists the change of current in the windings. In other words, if the current is pure DC current, the choke is not doing anything, so the choke does not affect the circuit. The moment the current tries to change, the choke intervenes and tries to prevent this change. If the current tends to decrease, the choke slows it from decreasing. Chokes are useful in electrical circuits precisely because of this feature. Rhuan and others (2017, p. 25) illustrate in their book that traditionally a choke has been used for converters with a high switching frequency to suppress harmonics. The high switching frequency of the converter is directly proportional to the IGBT switching losses of the semiconductors of the converter.

It is possible to influence the physical size of the filter by changing the switching frequency, which can correspondingly increase the amount of switching losses (Paakkinen, 2014, p. 33; Solanki & Yagnit, 2017, p. 1–2; Muhlethaler, 2012, p. 143; Haanpää, 2016, p. 2). However, increasing the switching frequency is limited, and the choke alone is not sufficient to meet the necessary damping requirements (Wang & others, 2003, p. 779).

As for the electrical symbol of the coil, in Figure 6a, when the current is constant, regardless of whether the current is 0 or some other value, the voltage across the coil will be equal to 0. As the current increases across the coil, in Figure 6b, the voltage has a certain value and is negative in the direction of current input and positive in the direction of output. In other words, it creates a potential difference across the coil, which tries to oppose the growth, thus trying to direct the current in the opposite direction. If the current decreases, then the voltage across the coil will be positive when viewed in the direction of current input and negative in the direction of output. This in turn sets the current in the same direction as the decreasing current, trying to prevent it from decreasing. In this way, the operation of the filter winding should be considered, and there is a potential difference between the windings only if the current changes.

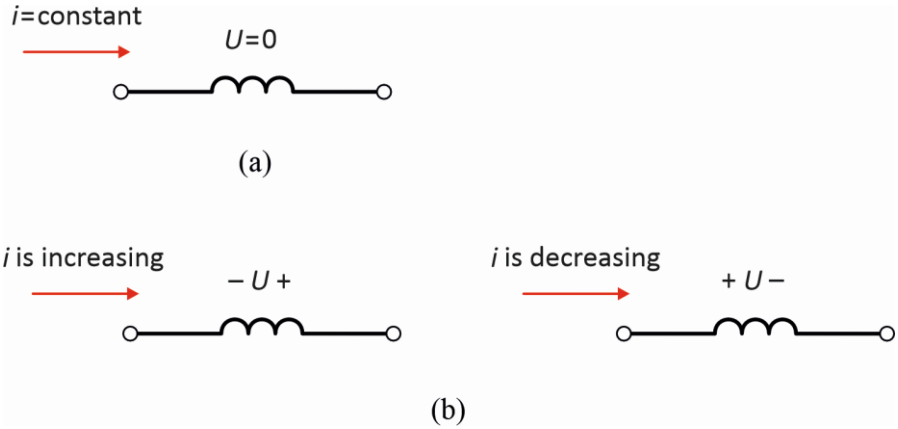

Figure 6. Current behavior in an inductor that normally opposes a change in current. The voltage across the inductor when the current is constant (a). The voltage across the inductor, as the current changes (b).

In the case where the inductance changes with time, thus the ratio of current to voltage across the inductance is calculated as follows

$$u_{\mathrm{L}}(t) = L \cdot \frac{di_{\mathrm{L}}(t)}{dt} \ . \tag{6}$$

Similarly, the LC filter is an improved version of the L filter, due to its ability to dampen better than L filter (Rhuan and others, 2017, p. 25). The transfer function of the filter is

affected by the type of suppress circuit selected (2017, p. 25). Similarly, like the L filter, at low frequencies the physical size of the LC filter increases and takes unnecessary space (Solanki & Yagnit, 2017, p. 1–2).

The LCL filter is designed to improve the power quality of the converter-based system and is mainly used to filter ripple currents and the filter itself also causes losses (International Electrotechnical Commission 61800-9-2 ED 2, 2021, p. 73; Loncarski, 2014 p. 11). In other words, the LCL filter effectively suppresses high-frequency current harmonics caused by the switching functions of the IGBT supply unit converter. The root cause of switching losses comes from the on and off state of the switches (Kartsonakis, 2021, p. 1). Current filtering takes place in such a way that the choke suppresses the ripple current or harmonic components created by IGBT switches, for example (Haanpää, 2016, p. 15). Thus, the advantage of the LCL filter can be considered a high suppress level (unwanted harmonics), a compact size, reduce the effect of noise, improves the quality of electricity, modify the frequency behaviour, limit the bandwidth of the signal and the ability to suppress without significant losses (Kumari, 2014, p. 8; Muhlethaler, 2012, p. 143).

Normally, the ripple current of the ISU is filtered by an LCL filter. Figure 7a shows the converter's base current (main current) and ripple current. The waveforms are sinusoidal. As far as the choke on the converter side is concerned, the increase in switching frequency can lead to an increase in current ripple. At higher frequencies, the losses begin to affect as the external $\boldsymbol{H}$-field changes. The result is that the high-frequency ripple current increases the amount of core losses and released heat, Rahman (2016, p. 4) emphasizes in his own research. Since the core losses are directly proportional to the high-frequency currents, the losses in the converter side inductor are greater than on the grid side (p. 8). This has a direct impact on the material selection of the iron core of the choke, which must withstand the heat rise caused by high frequency ripple current (p. 8). Correspondingly, this forces to consider the choice of components, where the choke on the converter side is more expensive than the choke on the grid side (p. 8). Looking more

closely at the ripple from the *BH* curve, a large loop is created for the basic waveform, and correspondingly at high frequencies a small loop is created, inside the loop of the basic waveform, as seen in Figure 7b (Muhlethaler, 2012, p. 4).

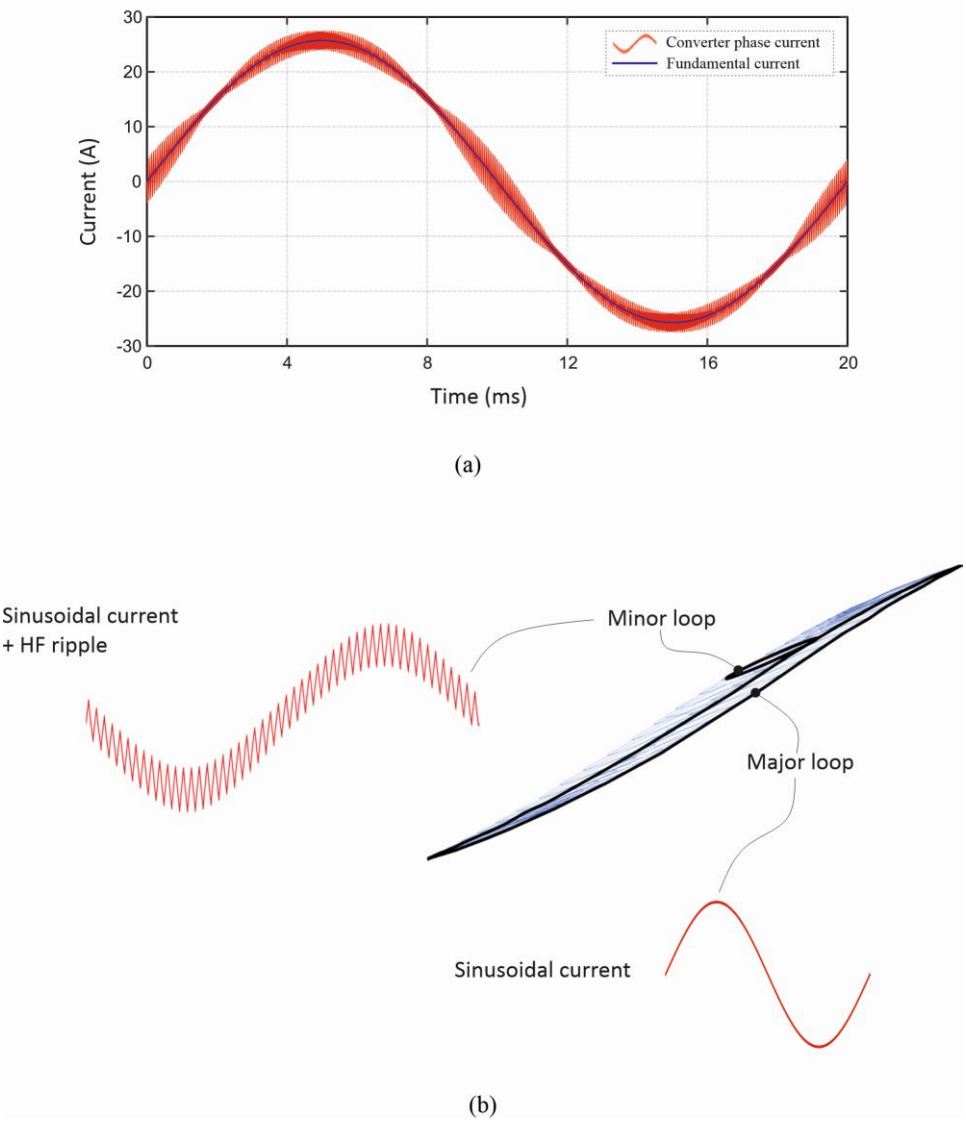

Figure 7. The ripple simulation current of the converter is compared to the fundamental current (a) (Rahman, 2016, p. 9). The *BH* curve illustrates the loss energy of a large loop, which originates from the fundamental waveform, and correspondingly, the loss energy of small loops originates from the high-frequency ripples (b) (Muhlethaler, 2012, p. 4).

2.2.2 Dynamic behavior of L, LC and LCL circuits: bode diagram

Kesarkar and Narayanasamy (2016, p. 1) illustrate in their own research text that the bode diagram linear model is a tool to help understand transfer function gain and transfer function phase angle. The purpose of Figures 8–10, pages 31–32 is to get a better understanding of the behaviour of L, LC, and LCL circuits. The vertical axis of the graph shows the transfer gain, $\boldsymbol{H}$ (s = jω), which is expressed in decibels, dB (p. 1–2). In other words, the magnitude of the transfer function is expressed in decibels. On the horizontal axis, there is a frequency, ω presented in logarithmic scale. The same thing is about the phase angle, where the vertical axis shows the phase angle, in degrees, and the horizontal axis shows the frequency, which is once again presented on a logarithmic scale. Finally, as for the bode diagram, the curves are replaced by direct approximations, where seven factors (such as constant gain, pole at the origin, zero at the origin, simple pole, simple zero, quadratic pole and quadratic zero) are treated separately and formed a single graphic representation of them (Kesarkar and Narayanasamy, 2016, p. 1–7); (Cheever, n.d).

Let's take a closer look at the graph in Figure 8. The curve shows that at low frequencies, when looking at the magnitude in decibels, dB, its magnitude is 0, which corresponds to 1. Thus, at low frequencies it is an overpass and correspondingly, when going to the highest frequencies, the curve goes towards negative values. In other words, the filter is a low-pass filter because it accepts all the lowest frequencies and then rejects all the higher frequencies. The low pass filter therefore enables the lowest signal frequencies. The frequencies start moving from DC to a smaller passable value and as the frequency's increases, the signal does not pass through the filter. As for the phase angle, when the gain is constant, then the phase angle is zero. At low frequencies magnitude = 0 dB (output = input). At high frequencies, output becomes small, magnitude = -30 dB. At low frequencies phase is near 0° and at high frequencies, phase is near -90°. As the gain decreases, the phase angle decreases and since the s-pole number is found in the denominator of the equation only once, the phase angle approaches -90° with increasing frequency.

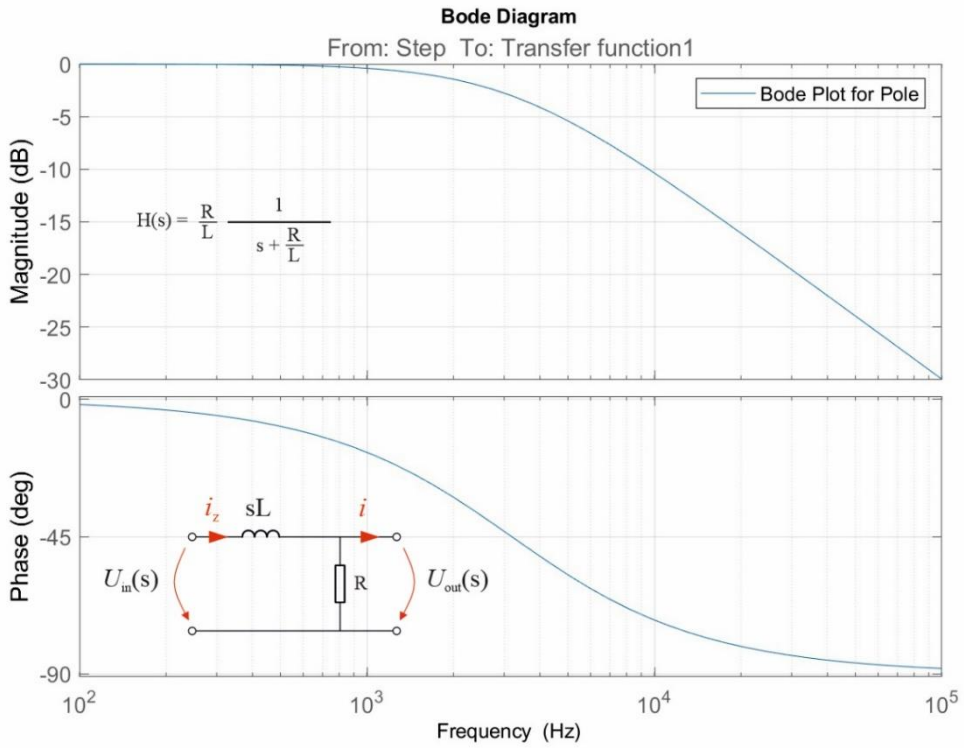

Figure 8. Bode diagram of L circuit.

As for the magnitude and phase plot curve shown in Figure 9, it is a low-pass filter. The graph shows that at low frequencies the gain is 0 dB, after which the gain decreases nonlinear as the frequency increases. At intermediate frequencies, the output becomes larger than the input and the maximum magnitude is about 13 dB. Thus, the resonance is located at a point where the magnitude is 13 dB. It can be seen from the phase graph that the curve decreases nonlinear with respect to the increasing frequency. The waving of the phase graph also indicates that the system is unstable. Figure 10 examines the dynamic behaviour of the LCL circuit. At low frequencies, the gain is zero. A sharp and high peak with a double pole can be seen in the middle frequencies, where the attenuation is at its maximum around 13 dB. After medium frequencies, the curve decreases as the frequency increases. Correspondingly, the phase diagram shows how at medium frequencies the curve makes a phase shift of -180°at the highest attenuation.

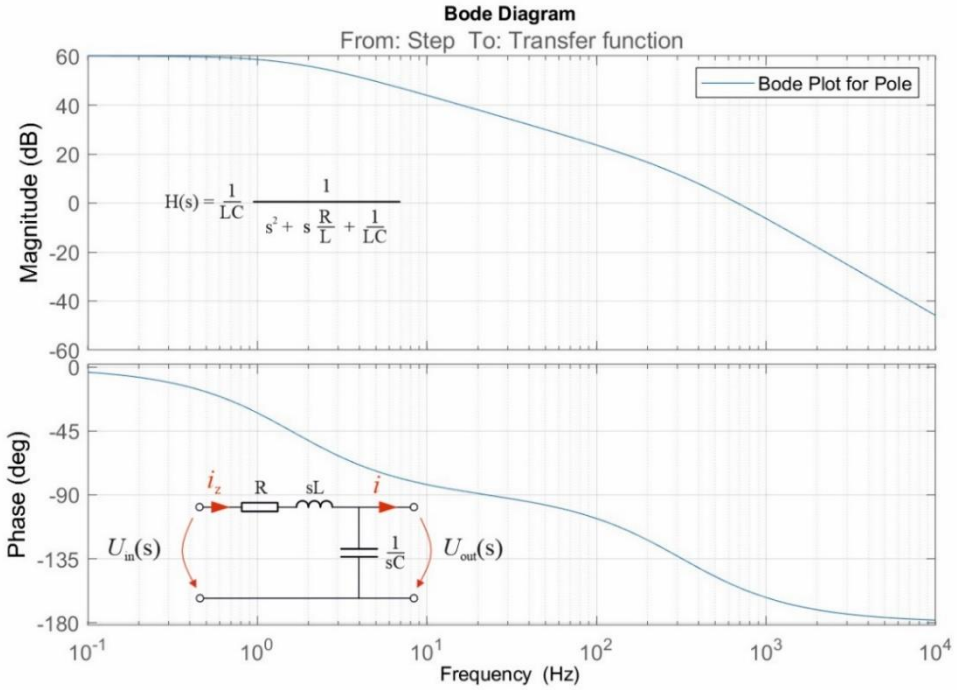

Figure 9. Bode diagram of LC circuit.

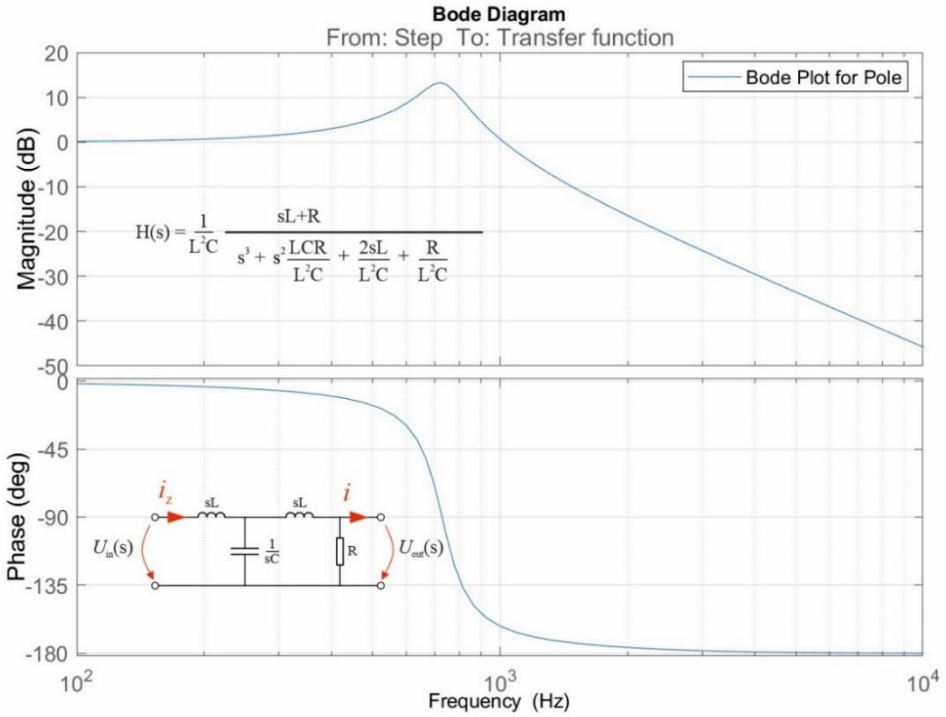

Figure 10. Bode diagram of LCL circuit.

The following logarithmic ratio is used for filter attenuation

$$\mathrm{a(dB)} = 20 \log_{10} \frac{i}{i_\mathrm{z}}, \tag{7}$$

where the attenuation of the filter structure is calculated by calculating the current, i passing through the circuit impedance, first without the filter and the second time with the filter, i_z (Albach & Fischer, 2020, p. 282).

Assuming constant component values at all frequencies, it can be seen from the graphs that the L filter provides 20 dB/dec, the second order LC filter provides 40 dB/dec, and the third order LCL filter provides 45 dB/dec. The results show that the LCL filter has the highest filtering capacity.

3 Choke winding

The current flowing through the windings of the choke causes losses in the windings due to their resistances. Calculation of losses requires information about the winding resistance. For direct current and low frequencies, this is simply determined by the cross-sectional area, length and resistivity of the conductor. At the highest frequencies (among other things 100 kHz), this is not the case, because the current is no longer evenly distributed over the cross-section of the conductor due to the skin and proximity effects (Muhlethaler, 2012, p. 113–114; Biela, 2011, p. 14–15). This chapter examines the physical phenomena that form losses and the necessary equations for calculating winding losses are defined.

3.1 Polarity of coils

The structure of core of the choke can be simple, if the core is single column, around which the winding passes and the flux,Φ has only one path. Correspondingly, when the core has more than two-columns (two coils), then the direction of the flux paths is presumably greater than two. In this thesis, a three-column choke is considered.

Figure 11 shows the core of a three-column choke. The coils are examined one at a time, assuming that all other coils are de-energized. Looking at Figure 11b, when the current I_1 flows downward around one of the pole windings, then the direction of the flux is thus upward. In case c, the current I_2 is fed to another coil. According to Figure 11c, the flux caused by it flows upwards through this coil and downwards through the other coils. Finally, in Figure 11d, the current, I_3 flows downwards along the winding conductor and correspondingly, the direction of flux is upward, which later branches and flows downwards through the winding.

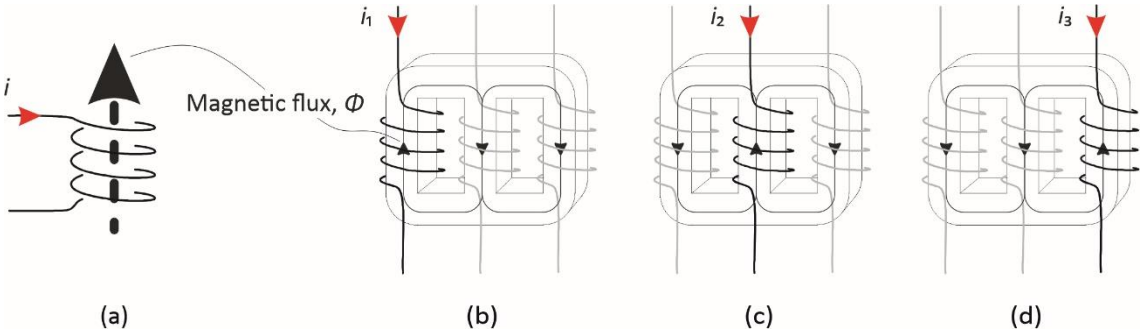

Figure 11. Polarity of windings. Inside the current winding, the direction of the flux it causes (a). If current, i_1 is applied to the winding, it causes a flux in the winding with the direction shown in Figure (b). The induced flux flows upward through this winding and downward through the other windings (c) and (d).

3.2 Foil conductor

Foil winding is a type of winding in which a foil conductor is used instead of a round conductor, which allows a large cross-section to be wound at once (Biela, 2005, p. 231). Muhlethaler (2012, p. 111) emphasizes that this winding type should be used in the case when the number of turns is low. The popularity of the foil winding is based on its ability to reduce eddy currents and thus high-frequency losses, and it is relatively inexpensive (p. 111). The disadvantages of the winding type include the increase in winding capacitance and the corrosion problem in case of the aluminium foil conductor when coming into contact with another metal (p. 111).

3.2.1 Skin and proximity effects

The architecture of the foil conductor is illustrated in Figure 12, where the current is infinite as it travels sinusoidally according to the right-hand rule, in the direction indicated by the thumb (x-direction). Figure 12 serves as a basis for calculation skin effect losses, and thus the values for the height, W_h and breadth, W_b of the conductor will be used in the analytical calculation.

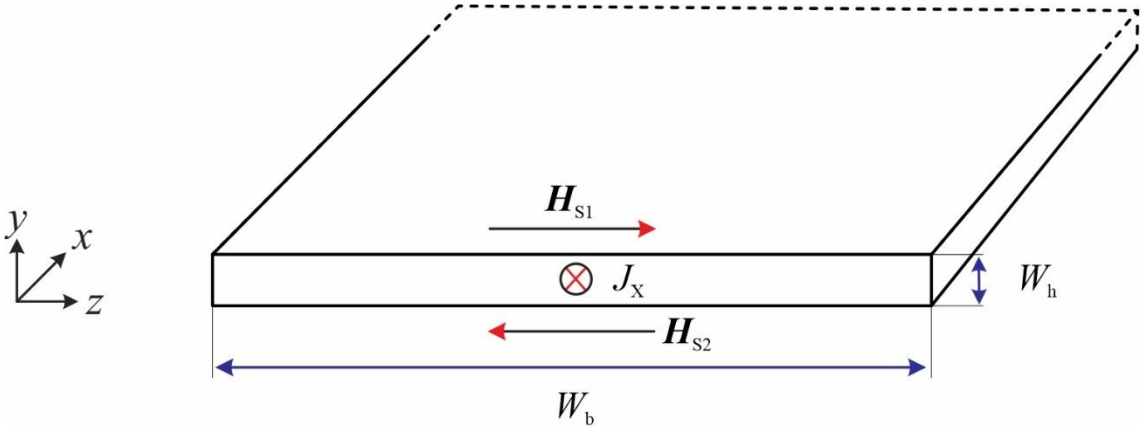

Figure 12. Current density and magnetic field in foil conductor. According to right-hand rule, the thumb indicates toward the current density, J_x, which is in same direction as unit vector $\boldsymbol{e}_x$, while the other fingers indicate toward the magnetic field strength, $\boldsymbol{H}$ (Biela, 2012, p. 29).

Figure 13 illustrates how an externally variable magnetic field with an amplitude $\boldsymbol{H}_s$ in the z direction operates on both sides of the foil conductor. The strength of the magnetic field, $\boldsymbol{H}_s$ travels parallel to the unit vector $\boldsymbol{e}_z$ along the breadth, W_b of the foil conductor.

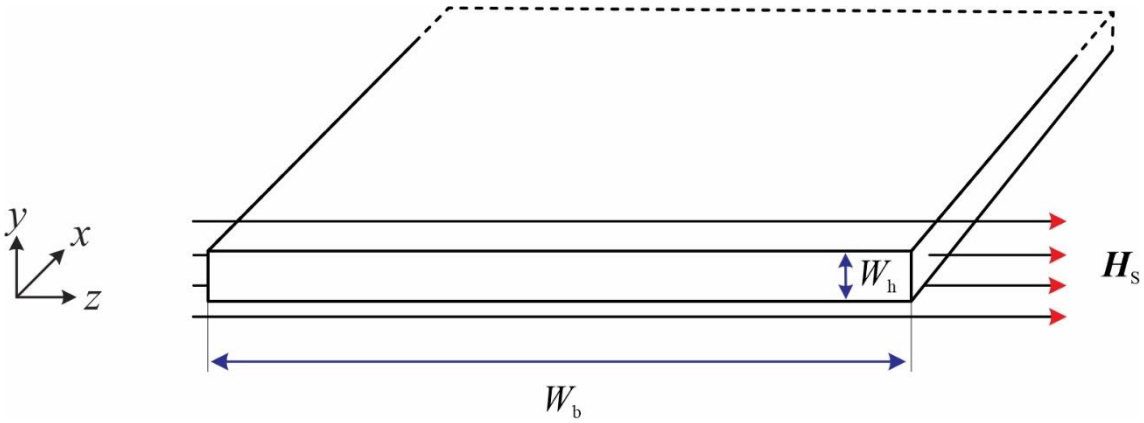

Figure 13. A cross-section of a foil conductor parallel to the unit vector ex. The amplitude of the $\boldsymbol{H}$-field, $\boldsymbol{H}_s$ acts in the direction of the unit vector $\boldsymbol{e}_z$ (Biela, 2012, p. 34).

3.2.2 Calculation of ohmic losses

Ignoring skin and proximity effects when calculating winding conductor losses leads to a deviation (error) (Dadafshar, 2012, p. 1). Initially, the resistance correction factor R_{f} should be calculated, which is later required to multiply the AC resistance and DC resistance of the winding to obtain the necessary AC resistance (Rahman, 2016, p. 35). When moving to the highest frequencies (for example kHz), the AC resistance of the coil is therefore high (Kazimierczuk & muut, 2004, p. 3). The ratio of the AC resistance, $R_{\mathrm{W(AC)}}$ of the winding as a function of frequency to the DC resistance, $R_{\mathrm{W(DC)}}$ can be calculated from the equation

$$R_{\mathrm{f}} = \text{(Skin effect)} + \text{(Proximity effect)}, \tag{8}$$

$$R_{\mathrm{f}} = A\left[\frac{e^{2A} - e^{-2A} + 2\sin(2A)}{e^{2A} + e^{-2A} - 2\cos(2A)} + \frac{2(N^2 - 1)}{3} \cdot \frac{e^{A} - e^{-A} - 2\sin(A)}{e^{A} + e^{-A} + 2\cos(A)}\right], \tag{9}$$

where N is the number of turns of the windings and the coefficient A is the cross-sectional area of the conductor which can be determined from equations 10, p. 37 or 11, p. 38 (Kazimierczuk & others, 2004, p. 3; Rahman, 2016, p. 35; Dadafshar, 2012, p. 1). The geometry of the round conductor is defined from the equation

$$A_{\mathrm{round}} = \left(\frac{\pi}{4}\right)^{\frac{3}{4}} \frac{d}{\delta}\sqrt{\frac{d}{P}}, \tag{10}$$

where d is the diameter of the round conductor and P is the distance between the centres of two adjacent conductors (Kazimierczuk & others, 2004, p. 3; Rahman, 2016, p. 35). Correspondingly, the geometry of the foil conductor can be determined from the following equation

$$A_{\mathrm{foil}} = \left(\frac{\pi}{4}\right)^{\frac{3}{4}} \frac{W_{\mathrm{h}}}{\delta} \sqrt{\frac{W_{\mathrm{b}}}{P}}, \tag{11}$$

where W_{h} is heigh of the foil conductor and W_{b} is breadth of the conductor as illustrated in Figure 12, page 36 and Figure 13, page 36 (Kazimierczuk and others, 2004, p. 3). The total power losses for a high-frequency AC winding conductor, where skin and proximity effects are taken into account, can be calculated from equation

$$P_{\mathrm{w}} = R_{\mathrm{f}} P_{\mathrm{W(DC)}}. \tag{12}$$

In order to predict the magnitude of the power loss, the DC resistance should be calculated (p. 1). According to Rahman (2016, p. 34), the ohmic losses of a DC winding without skin and proximity effects can be calculated using Ohm's law as follows

$$P_{\mathrm{w(DC)}} = I_{\mathrm{rms}}^2 R_{\mathrm{w(DC)}} \tag{13}$$

and for three-phase connection

$$P_{\mathrm{w(3p/DC)}} = 3 \cdot I_{\mathrm{rms}}^2 R_{\mathrm{w(DC)}}, \tag{14}$$

where the coefficient $R_{\mathrm{w(DC)}}$ is the DC resistance of the winding and the rms value of the winding current is I_{rms} (p. 34). The time dependent $\boldsymbol{H}$-field of the skin and proximity effects increases with frequency, simultaneously increasing the ohmic losses of the winding (p. 34).

3.2.3 Winding resistance

In order to calculate the relative resistance, the AC resistance of the winding should be determined. According to research by Dowell (1966, p. 1–5), the value of the AC winding resistance, $R_{\mathrm{w(AC)}}$ can be expressed as

$$R_{\mathrm{w(AC)}} = R_{\mathrm{w(DC)}}\left(M + \frac{\left(W_{\mathrm{N/layers}}^2 - 1\right)D}{3}\right), \tag{15}$$

where coefficient $W_{\mathrm{N/layers}}$ is the number of layers (number of whole layers in a winding portion) and factor M is the real part of complex number

$$M = Re(\alpha_{\mathrm{d}} W_{\mathrm{h}} \coth(\alpha_{\mathrm{d}} W_{\mathrm{h}})). \tag{16}$$

Correspondingly, factor D is the real part of complex number

$$D = Re\left(2\alpha_{\mathrm{d}} W_{\mathrm{h}} \tanh\left(\frac{\alpha_{\mathrm{d}} W_{\mathrm{h}}}{2}\right)\right) \tag{17}$$

(p. 1–4). Dowell's attenuation constant can be solved using the following equation

$$\alpha_{\mathrm{d}} = \sqrt{\frac{j\omega\mu_0\eta}{\rho_{\mathrm{T}}}}, \tag{18}$$

where eta, η is

$$\eta = \frac{W_{\mathrm{N/layer}} W_{\mathrm{h}}}{W_{\mathrm{b}}}, \tag{19}$$

and where factor $W_{\mathrm{N/layer}}$ is number of turns per layer and $\omega = 2\pi f$ (p. 1–5). The resistance of the DC winding can be calculated from the equation

$$R_{\mathrm{w(DC)}} = \frac{W_{\mathrm{N/layers}}\,\rho_{\mathrm{T}}\,N_{\mathrm{T/layer}}^{2}\,W_{\mathrm{mlt}}}{\eta W_{\mathrm{b}} W_{\mathrm{h}}}, \tag{20}$$

where W_{mlt} is mean length per turn, W_{h} is the height of winding conductor and W_{b} is breadth of conductor (p. 5).

As shown in Dowell's (1966, p. 5) study, the high frequency resistance of the AC winding can also be calculated using the following equation

$$R_{\mathrm{w(AC)}} = F_{\mathrm{R}} R_{\mathrm{w(DC)}} \tag{21}$$

where the ratio of the AC value of the winding resistance, R_{w} to the DC value is obtained from the following equation

$$F_{\mathrm{R}} = M + \frac{(W_{\mathrm{N/layers}}^{2} - 1)D}{3}. \tag{22}$$

3.2.4 Determination of inductance

Inductance is used to express its ability to store energy magnetically. Figure 14 examines a current loop for a better understanding. The current, $I(t)$ form a current loop that travels counter-clockwise according to the right-hand rule, with the other fingers pointing towards the resulting magnetic flux density, $\boldsymbol{B}(t)$. The formation of the $\boldsymbol{B}$-field is directly proportional to the value of the current.

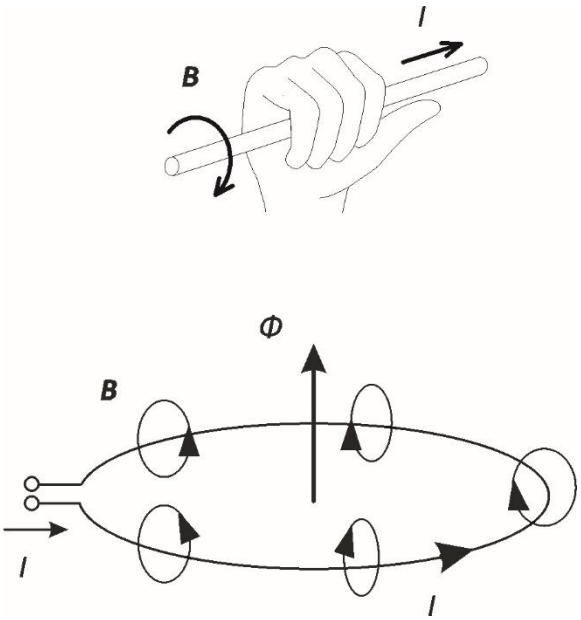

Figure 14. Illustration of a magnetic flux density, $\boldsymbol{B}$ generated by a current *I*.

The flux, Φ generated by the current, I is expressed by the inductance, L

$$\Phi = LI. \tag{23}$$

The flux, Φ flows through the entire area surrounding the wire loop, in other words it is the total flux connected to the coil. Regardless of the type of winding, the same flux passes through the winding. The flux, Φ can be calculated by multiplying the number of turns, N and the flux through the core, Φ_{core}

$$\Phi = N\Phi_{\mathrm{core}} \tag{24}$$

(Albach & Fischer, 2020, p. 207; Albach, 2020, p. 228). The ratio applies when calculating the inductance of the winding

$$L = \frac{N\Phi_{\mathrm{core}}}{I} = \frac{N^2\mu_{\mathrm{r}}\mu_0 A_{\mathrm{core}}}{l_{\mathrm{core}}} \tag{25}$$

(Kazimierczuk, 2014, p. 49, 52, 589; Albach, 2020, p. 226; Dauhajre & Middlebrook, 1986, p. 10). Correspondingly, the air gap inductance is obtained from equation

$$L = \frac{N^2 \mu_0 A_{\text{core}}}{l_{\text{gap}}}. \tag{26}$$

From the BH curve, as the core material approaches the saturation point, $\boldsymbol{B}_{\text{sat}}$, the permeability decreases, so the value of the inductance, L decreases in the same proportion. This issue can be solved by leaving an air gap in the core. The manufacturer normally states a so-called A_{L} value for each core, which is related to the material of the core and the air gap. The value of the inductance, L is directly dependent on the factor A_{L}

$$L = N^2 A_{\text{L}}, \tag{27}$$

which facilitates the dimensioning of the windings (Albach, 2011, p. 235). Based on the equation reviewed, the inductance factor A_{L} corresponds to the magnetic conductivity of the core or is inversely proportional to the reluctance of the core

$$L = \frac{N\Phi_{\text{core}}}{I} = \frac{N^2}{R_{\text{core}}} = N^2 A_{\text{L}} \tag{28}$$

and thus

$$A_{\text{L}} = \frac{1}{R_{\text{core}}}, \tag{29}$$

where the coefficient R_{core} is reluctance of the core (Hurley & Wölfe, 2013, p. 63, 68; Kazimierczuk, 2014, p. 49, 589; Multon & others, 2018, p. 10).

3.2.5 Temperature dependency of resistivity

The coefficient ρ is used for the resistivity of the conductor and it is usually proportional to the temperature (Kazimierczuk, 2014, p. 165). In other words, resistivity increases due to temperature and low resistivity leads to high eddy current losses (Erickson & Maksimovic, 2020, p. 424). Table 1 gives the resistivity and conductivity coefficients of different conductor materials, with a temperature of 20 C°, which corresponds to room temperature. Basically, the conductor material has an initial temperature, T_0 and final temperature, T, which is of interest.

Table 1. Resistance and conductivity specified for conductors at 20 °C (Kazimierczuk, 2014, p. 165).

Conductor material	Resistivity, ρ (Ωm)	Conductivity, σ (S/m)	Temperature coefficient, α (1/°C)
Aluminius (Ag)	2.65×10^{-8}	3.77×10^{7}	3.90×10^{-3}
Cobalt (Co)	6.24×10^{-8}	1.60×10^{7}	3.70×10^{-3}
Copper (Cu)	1.68×10^{-8}	5.96×10^{7}	4.04×10^{-3}
Gold (Au)	2.44×10^{-8}	4.11×10^{7}	3.40×10^{-3}
Iron (Fe)	9.70×10^{-8}	1.03×10^{7}	5.00×10^{-3}
Nickel (Ni)	6.99×10^{-8}	1.43×10^{7}	6.00×10^{-3}
Silver (Ag)	1.59×10^{-8}	6.30×10^{7}	3.80×10^{-3}
Zinc (Zn)	5.90×10^{-8}	1.69×10^{7}	3.70×10^{-3}

Typically, for aluminum the temperature dependence, $c_{\mathrm{Al(T0)}} = 0.0039\ (1/°\mathrm{C})$ from the initial temperature $(20\ °\mathrm{C})$. The resistivity, $\rho_{\mathrm{T}}\ (\Omega\mathrm{m})$ of the foil conductor at the final temperature T can be calculated from the following equation

$$\rho_{\mathrm{Al(T)}} = \rho_{\mathrm{Al(T_0)}} \cdot \left[1 + c_{\mathrm{Al(T_0)}} \cdot (T - T_0)\right] \tag{30}$$

(Hurley & Wölfe, 2013, p. 132; Chemie, n.d.; Ciptokusumo, p. 27; Romirer, p. 4; Kazimierczuk, 2014, p. 165).

4 Choke core

This chapter examines the principal structure of the core of the choke and the resulting losses. Typically, a core is made by assembling a core from cut sheets. To reduce eddy current losses, the sheets are insulated from each other by laminate. Due to the relatively high losses, the structure is primarily suitable for low frequencies. In general, core losses consist of hysteresis losses, eddy current losses and residual losses (formed by the relaxation mechanism), which depend on many influencing factors, such as the material used and the structure of the core (Zulk, 2021, p. 77, 98; Albach, 2017, p. 201–205). This problem greatly complicates the modeling of core losses. By reducing power losses, the choke's energy efficiency is increased and costs are minimized. Hysteresis losses are directly dependent on the frequency. Correspondingly, the formation of eddy current losses is influenced by a changing magnetic field that generates currents in the conductor. Residual losses strongly depend on temperature and thus the effect of core temperature must also be taken into account when the core material changes.

In power electronics, the dimensioning of the choke is usually based on the fact that it must withstand a certain current without becoming saturated and the losses must not cause excessive heating. These issues are taken into account when determining the core loss calculation.

4.1 The analogy between magnetic and electric circuit

This Section examines a magnetic circuit that is analogous to an electric circuit. Basically, the cores of the choke models discussed during this thesis are mainly three-column. The aluminium foil conductor is wound around the iron core pole turns, N. An AC current, I flows through the foil windings, so the core is magnetized by the magnetomotive force, $\mathrm{mmf}=F=NI$. The magnetomotive force, mmf

$$F = NI = \oint \boldsymbol{H} \cdot d\boldsymbol{l} \longrightarrow \begin{cases} \boldsymbol{H} = \dfrac{F}{l_{\mathrm{core}}} = \dfrac{NI}{l_{\mathrm{core}}} \\ \boldsymbol{H} = \dfrac{F}{l_{\mathrm{gap}}} = \dfrac{NI}{l_{\mathrm{gap}}} \end{cases}, \tag{31}$$

which acts as a source for the core causing a magnetic flux, Φ in the core, which can be obtained from the equation

$$\Phi = \frac{NI}{R_{\mathrm{core}}}. \tag{32}$$

In equations 31, page 45 and 32, page 45 the coefficient l_{core} is the average length of the core, l_{gap} is the average length of the air gap, and R_{core} is the reluctance of the core. The magnetic flux, Φ on the other hand, causes a magnetic flux density, $\boldsymbol{B}$ depending on the core cross-section, A_{core}, which is determined as follows

$$\Phi = \int \boldsymbol{B} \cdot d\boldsymbol{A} \tag{33}$$

and is solved from the equation

$$\Phi = \boldsymbol{B} A_{\mathrm{core}} \tag{34}$$

(Mclyman, 2004, p. 33; Rahman, 2016, p. 10).

The $\boldsymbol{H}$-field affects the $\boldsymbol{B}$-field through the magnetic response of the material in which the field is located. The magnetic field strength $\boldsymbol{H}$, whose unit is A/m, is given by the following equation

$$\boldsymbol{H} = \frac{\boldsymbol{B}}{\mu} = \frac{\boldsymbol{B}}{\mu_0 \mu_{\mathrm{r}}}. \tag{35}$$

In electromagnetism, a material usually tends to conduct flux, which is normally expressed by permeability, μ (Mclyman, 2004, p. 30). The magnetic permeability, μ_{r} increases as the temperature of core increases.

Figure 15b shows the electrical equivalent circuit of the entire core magnetic circuit, which fully corresponds to the circuit in Figure 15a. In the Figure 15, the material of the core and the air gap have their own reluctances defined. If each part of the core consists of a different material, then the material parts are defined with their own reluctances. When calculating the magnetic circuit, the equivalent circuit is defined according to the electric circuit, where magnetomotive forces, mmf are replaced by electromotive forces, $\mathrm{emf} = \boldsymbol{E}$, reluctances/resistances, $R_{\mathrm{core}}/R_{\mathrm{gap}}$ and magnetic fluxes, Φ with currents, I.

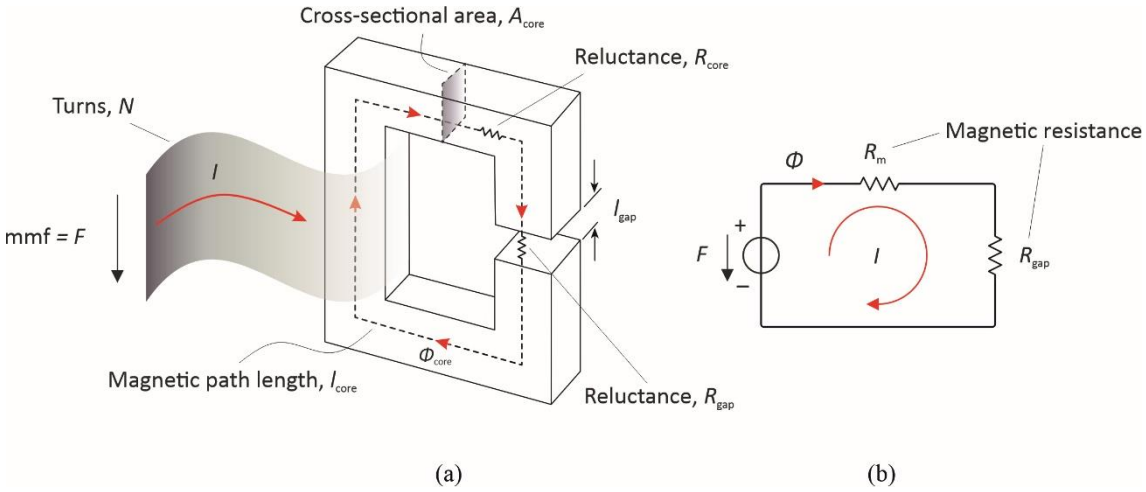

Figure 15. Typical choke core model consisting of a foil winding, a core and an air gap (a). The electrical equivalent circuit of the entire core magnetic circuit (b).

4.2 Core assembled from cut sheets to minimize eddy current losses

Figure 16 shows a choke core examined in calculation tools, assembled from cut sheets made of alloy steel and insulated by lamination to minimize eddy current losses. In other words, eddy current losses can be reduced by assembling the core from thin, insulated (laminated) cut sheets. The amount of eddy current losses can be reduced by assembling

the core from the cut sheets and isolating the cut sheets from each other, but eddy current losses cannot be completely eliminated. On the other hand, the architecture of the core can affect the magnitude of the magnetic flux spread. In Figure 16, the number of air gaps in the core per each column is 7 pieces. The breadth of the core cut sheet is 70 mm and the length of the laminated cut sheet pack is 110 mm.

According to Emetor (2022), lamination of cut sheets reduces the magnetic flux carrying capacity. Figure 16c shows the direction of the magnetic flux through the laminated cut sheets. The lamination (insulation) does not conduct magnetic flux and thus the cross-sectional area of the magnetic flux is smaller when passing through the conductor. The smaller cross-sectional area of the magnetic flux does not affect its magnitude (Emetor, 2022; Mclyman, 2004, p. 7–10).

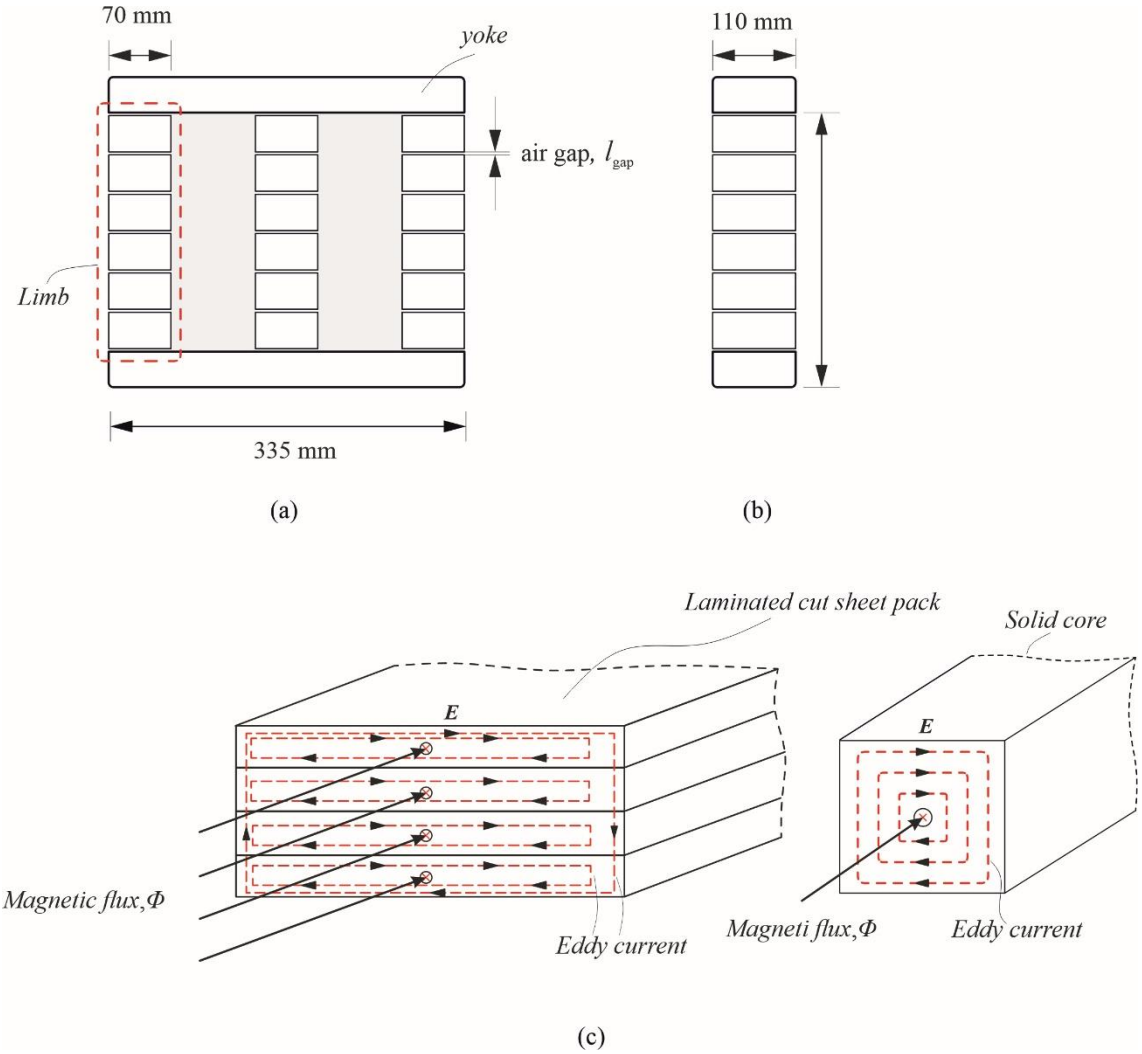

Figure 16. A core of the choke used in this thesis shown from the front and side (a) and (b). Insulation (lamination) between cut sheets is required to reduce eddy currents (c) (Mclyman, 2004, p. 108).

The cross-sectional area of the core is calculated from equation

$$A_{\text{core}} = b_{\text{Fe}} \cdot h_{\text{Fe}}, \tag{36}$$

where b_{Fe} is the breadth of the cut sheet (laminated pack) and h_{Fe} is the length of the laminated cut sheet pack. The cross-section of the core can differ at different parts, and in that case the parts of the core must be calculated separately. In addition, when determining the height, the air gaps of the limb should be subtracted from the final height.

The effective surface area (or net area) of a laminated pack consisting of cut sheets for the magnetic flux path can be calculated from equation

$$A_{\mathrm{core(eff)}} = Sf_{\mathrm{Fe}} \cdot A_{\mathrm{core}}, \tag{37}$$

where a stacking factor, Sf_{Fe} is used to express the ratio between cut sheets and lamination (Electrotekhnik, n.d.; Hurley & Wölfe, 2013, p. 109; Raina & Battacharya, 1991, p. 366).

Figure 16, page 48 and equation 36, page 48 provide the necessary information to calculate the volume of the core. Based on the initial data, the total core volume can be calculated using the following equation

$$V_{\mathrm{core}} = A_{\mathrm{core}} \cdot \left(2 \cdot Fe_{\mathrm{yoke}} + 3 \cdot Fe_{\mathrm{limb}}\right), \tag{38}$$

where the cross-sectional area of the core is A_{core}, the breadth of the yoke is Fe_{yoke} and the height of the limb is Fe_{limb}.

4.3 Temperature dependency of resistivity

The temperature dependency of the core is modelled by the coefficient c_{core}, which depends on the temperature and in a limited temperature range the temperature dependence of the core changes linearly compared to the temperature (Kazimierczuk, 2014, p. 165; Chemie, n.d.). As the temperature of the core material increases, the electron's movement shrinks, which in turn forces the temperature dependence of the core to increase (Kazimierczuk, 2014, p. 164–165).

Table 2. The material parameters of the choke prototype examined in this thesis.

	NUMERICAL VALUE
$c_{\text{core}}T_0$	-0.000907695
$k(H_{\text{DC}})$	8.00385
$\alpha(H_{\text{DC}})$	1.58022
$\beta(H_{\text{DC}})$	1.89937
T (°C)	150
T_0(°C)	20

The temperature dependence of the core, c_{core} from the final temperature, T can be calculated by using the values in Table 2

$$c_{\text{core(T)}} = 1 + c_{\text{core}(T_0)}(T - T_0), \tag{39}$$

where T_0 is the ambient temperature (Hurley & Wölfe, 2013, p. 63; Kazimierczuk, 2014, p. 165; Chemie, n.d.).

4.4 Definition of saturation magnetic flux density

Figure 17 illustrates the current waveform (ripple), which is directly proportional to the magnetic flux density, $\boldsymbol{B}$. The peak value of the current is $I_{\text{peak}} = \sqrt{2} \cdot I_{\text{rms}}$ and the rms value is I_{rms}. The amplitude is the maximum value of current or voltage. The current ripple or in other words the peak-to-peak amplitude is $2\Delta I$ and its alternating component is ΔI. The magnetic flux density ripple is $2\Delta\boldsymbol{B}$, which is peak-to-peak amplitude, and the peak value of its alternating component is amplitude $\Delta\boldsymbol{B}$ and the peak value is $\boldsymbol{B}_{\text{peak}}$. The frequency of the alternating current component is f.

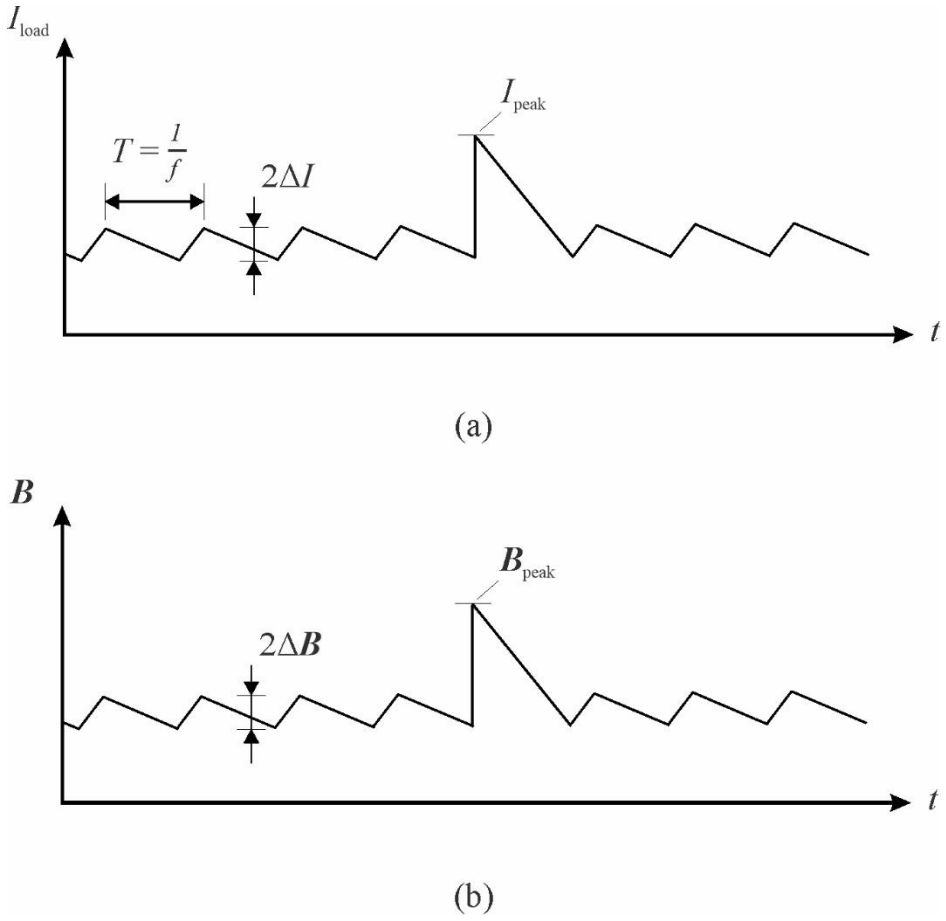

Figure 17. Illustration of the current waveform with ripple. The load current versus time is examined at (a) and the magnetic flux density versus time at (b).

In order to calculate the loss calculation of the choke core, it is necessary to find out the peak value ΔI of the $2\Delta I$ alternating component of the current ripple. The peak value of the alternating component of flux density, $\Delta \boldsymbol{B}$ can be calculated as follows

$$\Delta \boldsymbol{B} = \frac{\boldsymbol{B}_{\text{peak}}\,\Delta I}{I_{\text{peak}}} = \frac{\Delta I}{A_{\text{core(eff)}}}\sqrt{A_{\text{L}}L} = \frac{N\Delta I A_{\text{L}}}{A_{\text{core(eff)}}}, \tag{40}$$

where the coefficient A_{L} is $^{1}/_{R_{\text{m}}}$. In the previous equation, the cross-sectional area of the core should be considered, which can be the minimum cross-sectional area, A_{core} or the effective cross-sectional area, $A_{\text{core(eff)}}$. Normally, the minimum cross-section area

of the core is smaller than the effective cross-sectional area. In general, if the core sheet layers are laminated, an effective cross-sectional area is used.

An increase in the temperature of the core leads to losses, which partly limits the peak value of the magnetic flux density, $\boldsymbol{B}_{\mathrm{peak}}$ (Hurley & Wölfe, 2013, p. 10–13; Kazmierczuk, 2014, p. 587). In addition to this, the peak value of the magnetic flux density is limited by the saturation of the core (Kazmierczuk, 2014, p. 587). In other words, the magnetic flux density, $\boldsymbol{B}_{\mathrm{peak}}$ is limited by the maximum allowed flux density of the core material, $\boldsymbol{B}_{\mathrm{peak}} < \boldsymbol{B}_{\mathrm{sat}}$ (Hurley & Wölfe, 2013, p. 7–8).

Zach (2015, p. 1937) clarifies that when the situation in Figure 17, page 51 is examined more closely from the BH curve, the magnetic flux density of the core, $\boldsymbol{B}$ reaches the saturation flux density, $\boldsymbol{B}_{\mathrm{sat}}$. Thus, the current in the winding has a direct effect on the magnetic flux density, $\boldsymbol{B}$. When calculating the saturation characteristic of the core, the maximum current must be determined, which is also the operating current of the choke (p. 1937–1938).

According to Rantanen's thesis (2017, p. 29–30), the design of the choke should take into account the fact that the choke does not get saturated. Thus, the choke must be able to withstand a current that does not lead to saturation, $\boldsymbol{B}_{\mathrm{sat}}$. In addition, efforts should be made to avoid choke losses, so that they do not lead to overheating of the choke (p. 29–30). In other words, it must be possible to supply a certain maximum current to the LCL filter without saturation. Normally, when determining the required calculations of the choke, the maximum current, I_{max} should be rounded by 10 % at the definition stage to avoid the choke interference, aging, and current peak problems (p. 29–30). From the *BH* curve, the saturation current may be exceeded due to alternating current ripple, regardless of whether the DC current remains below the saturation point (p. 30). The saturation of the magnetic flux density of the core can be calculated from equation

$$\boldsymbol{B}_{\mathrm{sat}} = \frac{L I_{\max}}{A_{\mathrm{core}} N} \tag{41}$$

where the winding current, $I_{\max}$ is the highest amplitude at which the core saturates, the coefficient $\boldsymbol{B}_{\mathrm{sat}}$ is the maximum saturation flux density at $I_{\max}$, and A_{core} is the cross-sectional area of the core (Kazmierczuk, 2014, p. 32, p. 449, 589; Rantanen 2017, p. 29–30).

4.5 Typical model for calculating core losses

According to a recent study by Stenglein (2021, p. 14–15), there are several ways in the literature to calculate core losses that can be used to study and describe material behaviour. C. P. Steinmetz divides core losses into classic and modern core loss models (p. 14–15). When it comes to classic core losses, Steinmetz focuses on eddy current losses, which are affected by the architecture of the core (p. 15). Similarly, modern core loss models focus on the core material and eddy currents, which are directly proportional to the architecture of the core (p. 15). Due to a limited schedule, the focus of this master's thesis is on a simplified core loss model.

Typically, the Steinmetz loss model is used to describe the process of the core material (Zach, 2015, p. 1915). This Section examines in more detail the simplified Steinmetz loss calculation model, which will also be utilized in the analytical calculation model.

Usually, the manufacturer provides the necessary tables showing the required core losses, as losses are very difficult to calculate numerically. The purpose of this thesis is to find out losses through numerical calculation. According to Zach's research paper (2015, p. 1915), core losses can be calculated using the following formula

$$P_{\mathrm{core}} = V_{\mathrm{core}} \left(c_{\mathrm{core(T)}}\, k(H_{\mathrm{DC}})\, f^{\alpha(H_{\mathrm{DC}})}\, \Delta B_{\mathrm{AC}}^{\beta(H_{\mathrm{DC}})} \right), \tag{42}$$

where the variable V_{core} is the total volume of the core, $c_{\mathrm{core(T)}}$ models the temperature dependence of the final temperature, T (Zach, 2015, p. 1915, 1922). The coefficient $k_{\mathrm{H(DC)}}$ is a constant for a certain core material and the frequency, f term describes the dependence of the winding sine wave on the $\boldsymbol{H}$-field. The coefficients $k(H_{\mathrm{DC}})$, $\alpha(H_{\mathrm{DC}})$, $\beta(H_{\mathrm{DC}})$ are material coefficients and model losses as a function of frequency (Zach, 2015, p. 1915, 1922; Kazmierczuk, 2014, p. 129). Material coefficients are constants for a certain core material and can be found on the manufacturer's website or must be matched to material coefficients through calculations. Factor $\Delta B_{\mathrm{(AC)}}$ is the amplitude of the sinusoidal component of magnetic flux density (Zach, 2015, p. 1915, 1922; Biela, 2005, p. 299; Kazmierczuk, 2014, p. 129). The temperature dependence, c is modelled from equation 39, page 50.

5 Results and evaluation

The aim of this thesis is to develop two analytical calculation models to support the design of the main circuit for determining core and winding losses. This chapter examines the design process of the analytical calculation tools and which equations from the theory part have been utilized in the calculation tools. Analytical calculation models are developed in such a way that their operation is based on user input values, which are used to determine the calculation results that have been identified as important. Based on these results, it is possible for the designer to estimate the total losses and find the best possible solution for the operation of the converter.

In this chapter, simulations using FEMM 2D software are made for one filter model. Simulations are needed to verify the accuracy of the analytical calculation models. As part of the work, the aim is to verify the operation of the calculation models by performing simulations. Finally, conclusions are made about the simulation results and their significance is evaluated.

5.1 Choke modeling using simulation software

Figure 18 takes a closer look at the physical model of the choke using 2D simulation software. The choke-based filter consists of three foil windings connected in parallel and the core is made of alloy steel. The foil winding is made of aluminum, the number of turns is 12.5 and the thickness is 1 mm. The number of air gaps per each column is 7 pieces. Let's examine the first winding from the left side of the choke in Figure 18. When the current i_1 is applied, it causes a magnetic flux in the core, which flows upwards. The magnetic flux goes upwards through the first coil and continues down through the other coils. The strength of the magnetic field, $\boldsymbol{H}$ is at its lowest when the relative permeability of the substance, μ_r is high, this can be examined from equation 35, page 45. The simulation result shows that the $\boldsymbol{H}$-field strength is at its highest in air gaps and winding areas.

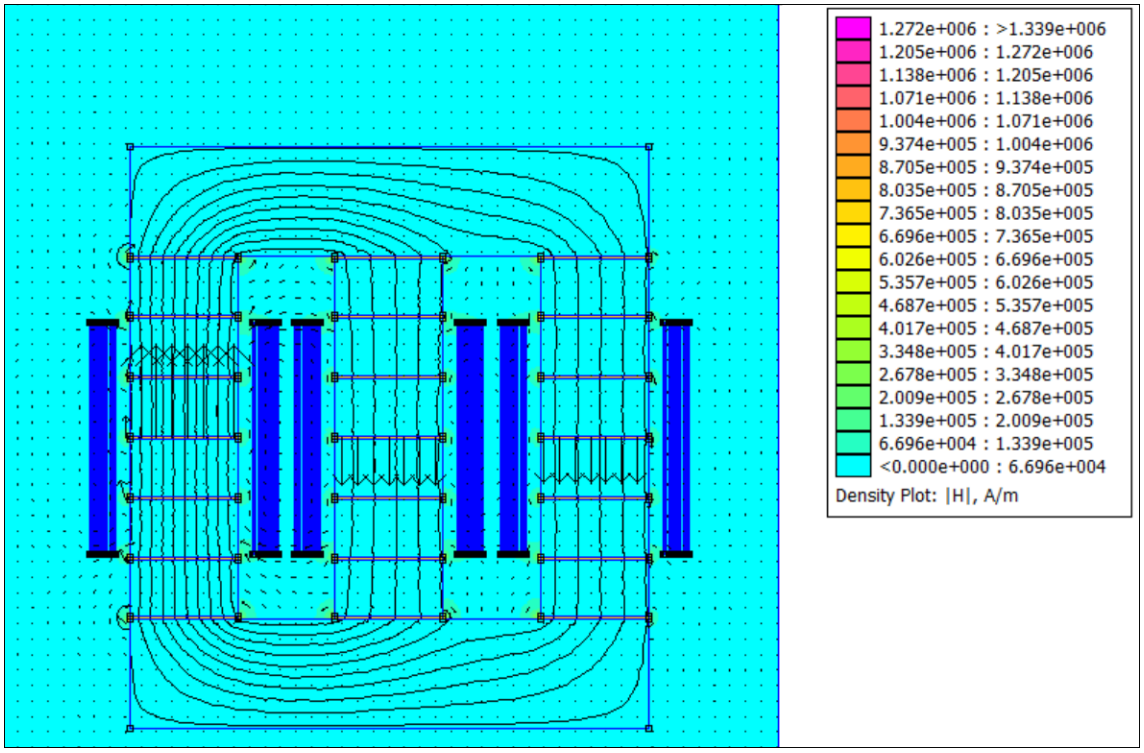

Figure 18. A core with an induced magnetic flux due to an AC current of 652 A on the left-hand of the limb and a frequency of 50 Hz.

As can be seen from Figure 19, the core is saturated steadily. The uniform red color which represents the maximum value is mostly in the core. Except for the air gaps, the magnitude of the magnetic field is smallest in the blue corners. This can be explained by the fact that the magnetic flux tends to travel around the core along the shortest path.

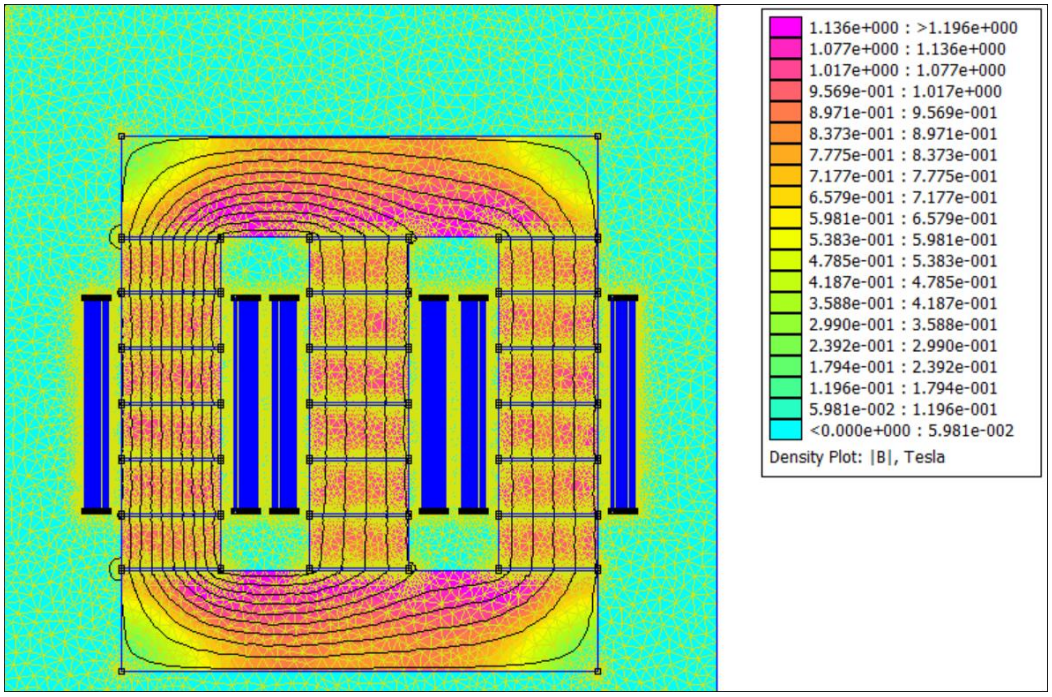

Figure 19. Magnetic flux density distribution of choke-based core saturated with 652 A AC current at a frequency of 50 Hz.

Typically, the root cause of winding losses comes from the winding current, which is not the only source of winding losses. Figure 20 shows the simulated magnetic flux density, $\boldsymbol{B}$ distribution and as can be seen from the figure, the magnetic flux density, $\boldsymbol{B}$ increases as approaching the winding. Fringing flux is formed at the air gaps of the core, which increases the inductance of the winding and thus the flux and saturation of the core. The magnitude of the fringing flux is directly proportional to the length of the air gap. Based on the figure, the fringing flux extends into the winding area and according to the theory part, eddy currents and thus additional losses are formed. By increasing the distance between the air gaps and the windings, and by reducing the frequency from 10 kHz to 50 Hz, the strength of the magnetic flux density decreases, which is directly proportional to the losses of the windings.

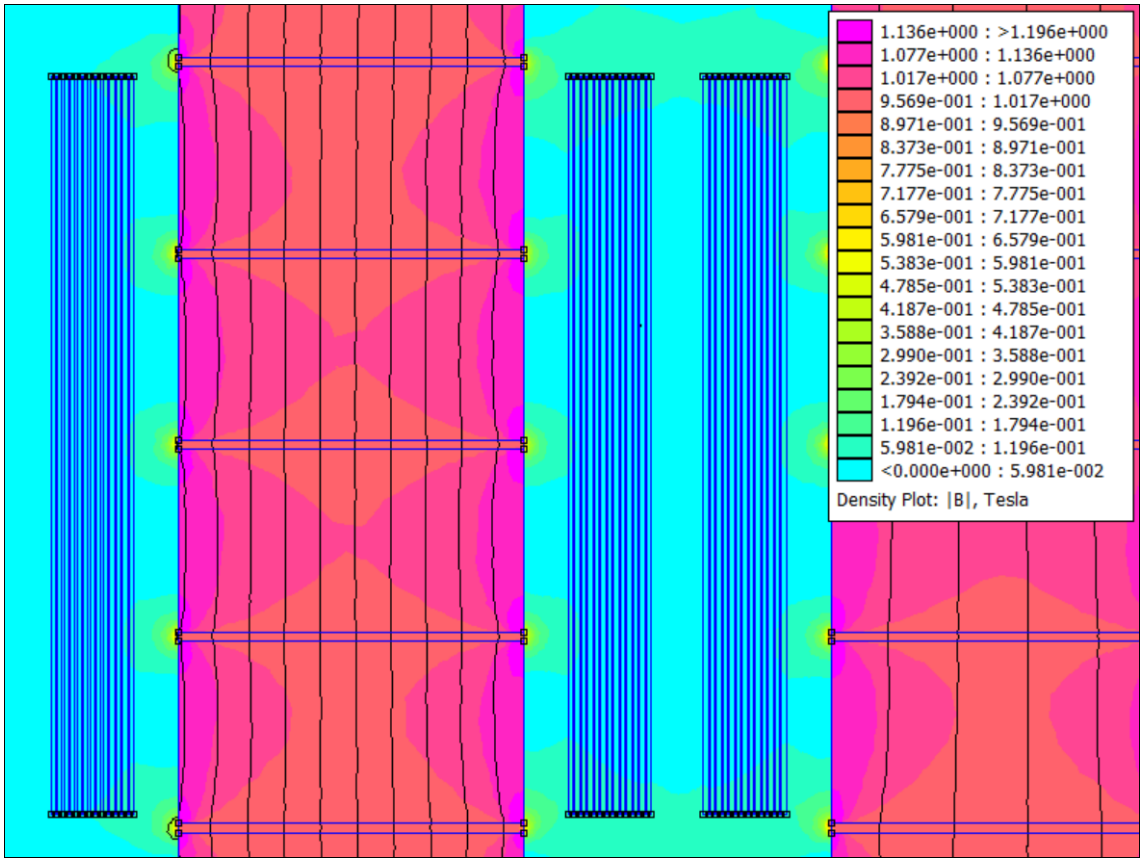

Figure 20. The magnetic flux density, $\boldsymbol{B}$ is highest in the air gaps and extends to the winding area, causing eddy currents and additional losses in the windings.

5.2 Design of analytical loss calculation models

Next we examine the design process of developed calculation models. Both analytical calculation models were developed in the MATLAB environment by utilizing the equations discussed in the theory part. In Section 5.2.1, the analytical calculation model for calculating core and winding losses is examined. The Section 5.2.2 examines the analytical calculation model for calculating AC winding losses. The difference between the two analytical loss calculation tools is that the first analytical loss calculation tool (Appendix 1) does not use FEMM 2D simulation software and the loss result is based entirely on numerical calculation. FEMM 2D simulation software is used to simulate the required winding losses in a 2D environment, which are further refined to determine losses in a 3D environment.

5.2.1 Analytical loss calculation model for calculating AC winding and core losses

This section discusses the core and winding loss calculation tool, which can be found from Appendix 1. The tool was designed in the MATLAB environment, where the losses are calculated numerically using the necessary equations. Later, the numerical calculation was developed as a MATLAB application tool. The application works in such a way that the numerical calculation is programmed to print a pop-up window showing the relevant equations. The pop-up shows the choke core and winding losses. The essential variables can be edited directly from the pop-up window, such as the frequency range and the rms value of the current, as can be seen from Figure 21. Frequency converters generally operate using the switching frequency in range of 1 to 18 kilohertz (kHz). Thus, the losses are defined in six different frequency points from 50 Hz up to kilohertz (kHz). As shown in Figure 21, the input data of dimensioning is, in addition to the frequency, the effective value of the current (rms current) in six different operating points.

VARIABLE PARAMETERS of CHOKE	FREQUENCY, f [Hz]		rms, [A]
FREQUENCY, f_1	50	NOMINAL, rms VALUE of the WINDING CURRENT, W_Irms_1	461.4
FREQUENCY, f_2	3636	NOMINAL, rms VALUE of the WINDING CURRENT, W_Irms_2	39.5
FREQUENCY, f_3	7273	NOMINAL, rms VALUE of the WINDING CURRENT, W_Irms_3	11
FREQUENCY, f_4	1.091e+04	NOMINAL, rms VALUE of the WINDING CURRENT, W_Irms_4	3.3
FREQUENCY, f_5	1.454e+04	NOMINAL, rms VALUE of the WINDING CURRENT, W_Irms_5	2.9
FREQUENCY, f_6	1.818e+04	NOMINAL, rms VALUE of the WINDING CURRENT, W_Irms_6	0.5

Figure 21. Definition of variables such as frequency and effective current.

In the first step of the analytical loss calculation model, the core cross-sectional area and the effective cross-sectional area were determined, which were obtained from equations 36, page 48 and 37, page 49. Based on this information, the core volume could be determined, which was obtained using equation 38, page 49. The choke considered in this calculation consists of three limbs and two yokes, similarly as in Figure 16, page 48.

The number of turns can be determined from equation 41, page 53, as shown in Figure 22. The input data for the calculation are the inductance, L, the peak current of the winding, $I_{\max}$, and the maximum of the magnetic flux density, $\boldsymbol{B}_{\max}$. The effective cross-sectional area of the core, $A_{\mathrm{core(eff)}}$ is obtained from equation 37, page 49. The peak current of the winding, which is also the saturation current, $I_{\max} = I_{\mathrm{sat}}$ corresponds to the magnetic flux density, $\boldsymbol{B}_{\max} = \boldsymbol{B}_{\mathrm{sat}}$.

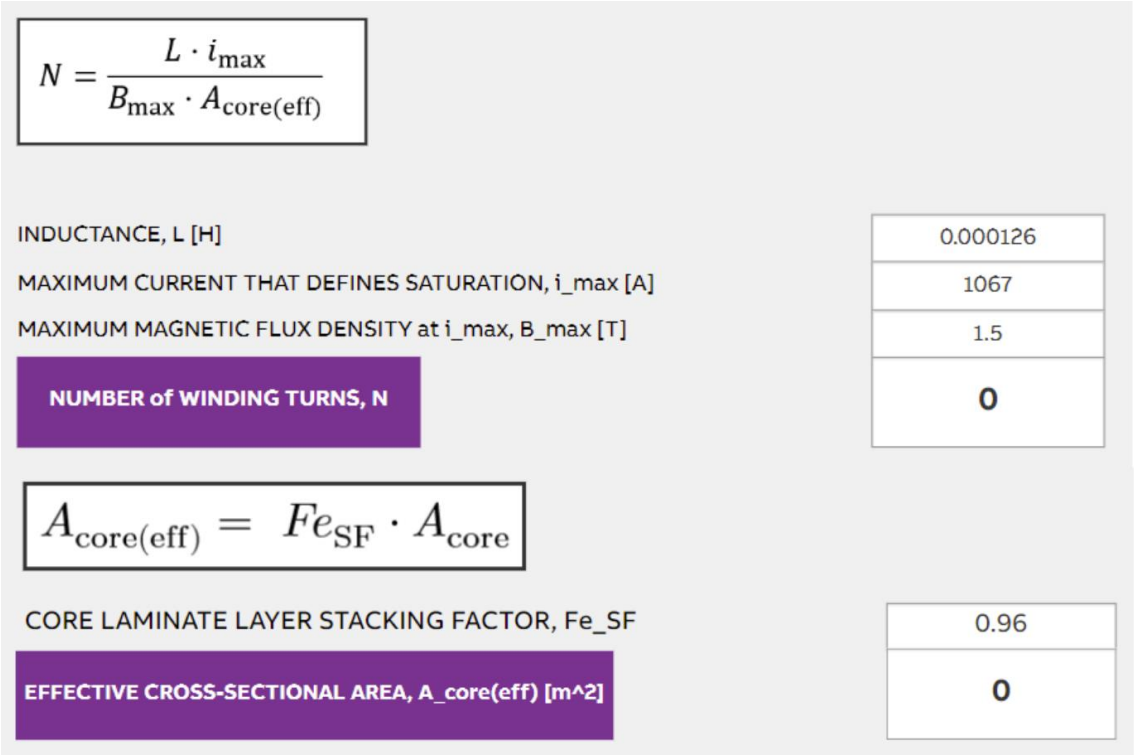

Figure 22. The equation required to calculate the winding turns and the effective cross-sectional area of the core.

If the saturation flux density of the core material is known, then the number of windings turns can also be calculated from the equation

$$N = \frac{\boldsymbol{B}_{\mathrm{sat}} l_{\mathrm{core}}}{\mu_{\mathrm{r}} \mu_0 i_{\mathrm{max}}}. \tag{43}$$

Figure 23, shows the equation for the peak value of the AC component of the magnetic flux density required for core loss calculation as defined in equation 40, page 51. Typically, if the core flux contains an alternating component, losses occur in the core for various reasons. These consist mostly of hysteresis and eddy current losses. The calculation is based on the number of windings turns, N peak current value, I_{peak} A_{L} value and the effective surface area of the core. The A_{L}-value is defined from equation 29, page 42.

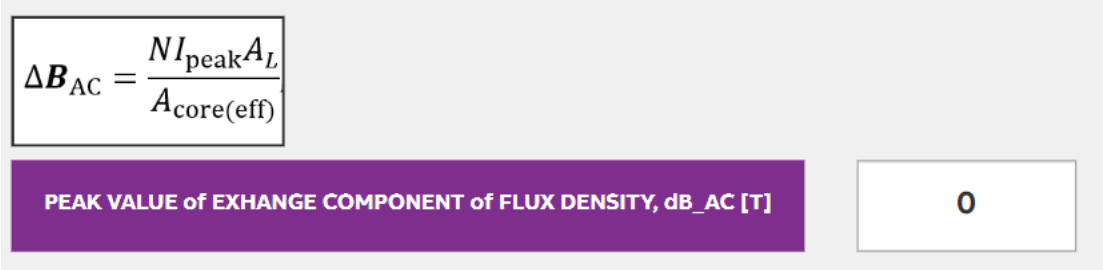

Figure 23. Amplitude of AC component of magnetic flux density.

The resistivity of the conductor from the final temperature as defined in Figure 24, basing on equation 30, page 43. The operating temperature of the choke winding is set to the highest level. In addition, as the size increases, the internal heating of the component increases, so the internal temperature is higher than the surface temperature. Here, the choke temperature is 150 °C and the ambient temperature is 20 °C. The initial data, such as the resistivity of the conductor material from the initial temperature and the temperature dependence, are known.

$$\rho_{\mathrm{Al(T)}} = \rho_{\mathrm{Al(T_0)}} \cdot \left[1 + c_{\mathrm{Al(T_0)}} \cdot (T - T_0)\right]$$

RESISTIVITY of the CONDUCTOR, ρ_T0 FROM the INITIAL TEMPERATURE, T_0 [Ωm]	2.65e-08
TEMPERATURE DEPENDENCE, c_(T_0) [°C]	0.0039
INITIAL TEMPERATURE, T_0 [°C]	20
FINAL TEMPERATURE, T [°C]	150
RESISTIVITY of the CONDUCTOR, ρ_T FROM the FINAL TEMPERATURE [Ωm]	**0**

Figure 24. Determination of conductor resistivity.

The equation in Figure 25 is used to calculate the volume of the conductor. The equation is later required to calculate the volume loss density of the winding. The starting data for the calculation are the conductor's cross-section, length, number of turns and average length per turn.

$$W_{\mathrm{V}} = W_{\mathrm{A}} W_{\mathrm{length}}$$

VOLUME of CONDUCTOR, W_V [m^3]	**0**

Figure 25. The equation used to determine the volume of a winding conductor.

The current flowing through the windings causes losses in the windings due to resistance. Therefore, to calculate the losses, the initial information about the winding resistance is needed. The calculation of the direct current resistance of the conductor, which is illustrated in Figure 26, is defined in more detail in equation 19, page 39. For direct current and low frequencies, the direct current resistance can be determined when the height and breadth of the winding conductor, the Dowell porosity factor, the number of windings turns, the resistivity of the conductor from the final temperature and the average length of the winding per turn are known.

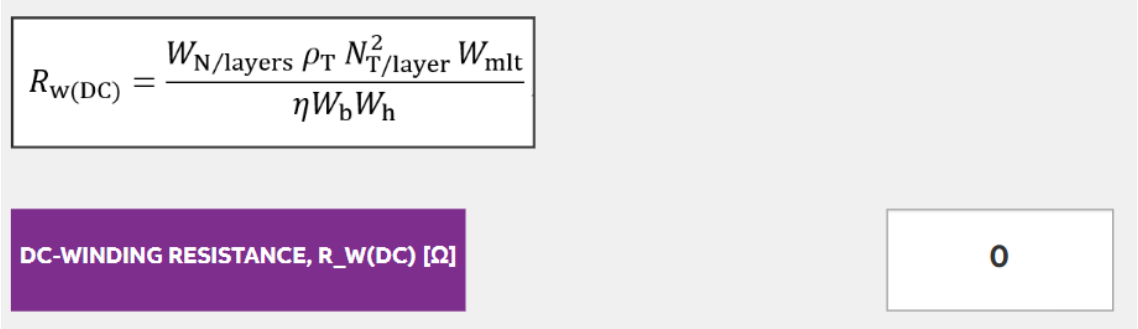

Figure 26. Determination of DC winding resistance.

The calculation of the alternating current resistance of the winding, which is illustrated in Figure 27, is defined in more detail in equation 21, page 40. Due to the proximity effect, the winding resistance depends on the geometry of the windings and their mutual geometry. When the current is not sinusoidal, in order to determine the losses, the alternating current resistance of the winding must be calculated for each significant frequency component of the current separately and the partial losses calculated from these must be combined. Relative resistance is defined from equation 24, page 41.

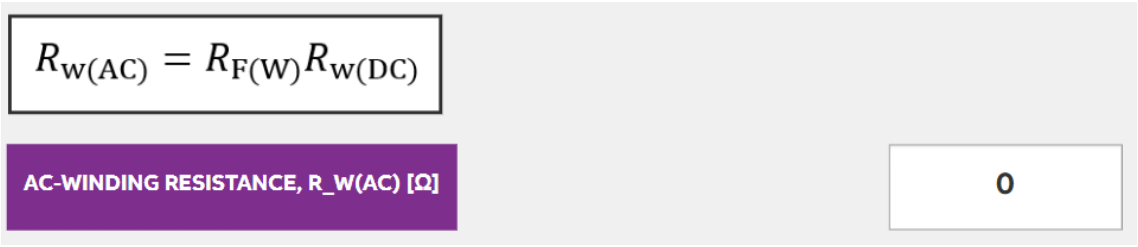

Figure 27. Determination of AC winding resistance.

The temperature dependence of the core from the final temperature, which is illustrated in Figure 28, is defined in more detail in equation 39, page 50. In the calculation, the ambient temperature of the core, as well as the operating temperature, must be taken into account. In general, the size of the component affects the final temperature. If the size of the core increases, then the internal temperature increases. The internal temperature is higher than the external temperature. The value of the temperature dependence coefficient for the initial temperature is given in Table 2, page 50.

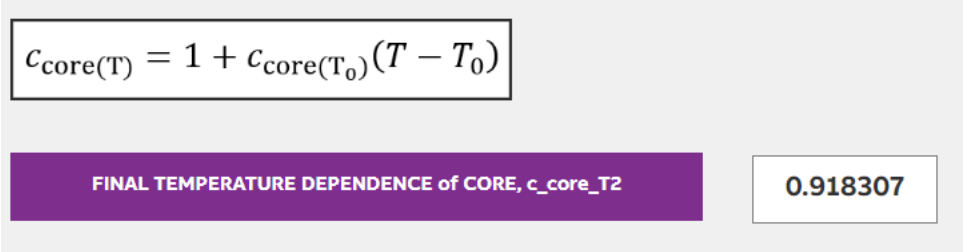

Figure 28. Determination of the temperature dependence of the core from the final temperature.

The power loss of the core is examined in Figure 29. The Steinmetz equation used in the loss calculation of the core is defined in more detail in equation 42, page 53. Loss parameters such as empirical coefficient, attenuation coefficient and phase constant are material coefficients obtained directly from the loss curves. In addition to the material factors, other input data for the calculation of core loss are the core volume, frequency and the peak value of the AC component of the magnetic flux density. If the amplitude and frequency of the alternating component of the flux are large, the core losses form a significant part of the total choke losses. The aim here is to examine losses in six different frequency values from 50 Hz up to 18.2 kHz frequencies. Based on the results, total losses decrease linearly relative to increasing frequency. If the frequency is reduced to prevent the flux density component from increasing, then core losses are reduced.

$$P_{\text{core}} = V_{\text{core}} \left(c_{\text{core(T)}}\, k(H_{\text{DC}})\, f^{\alpha(H_{\text{DC}})}\, \Delta B_{\text{AC}}^{\beta(H_{\text{DC}})} \right)$$

EMPIRICAL COEFFICIENT, k(H_DC)	8.004
ATTENTUATION COEFFICIENT, α(H_DC)	1.58
PHASE CONSTANT, β(H_DC)	1.899
CORE LOSS, P_core_f1 [W]	0
CORE LOSS, P_core_f2 [W]	0
CORE LOSS, P_core_f3 [W]	0
CORE LOSS, P_core_f4 [W]	0
CORE LOSS, P_core_f5 [W]	0
CORE LOSS, P_core_f6 [W]	0

Figure 29. Determination of core losses by using the Steinmetz equation.

Winding losses in six different frequency ranges are examined in Figure 30 and the equation used is defined in more detail in equation 14, page 38. The calculation of winding losses requires information about the rms value and the AC winding resistance. A large part of the winding losses is alternating current losses and the core of the choke considered here is wound by three foil windings connected in parallel.

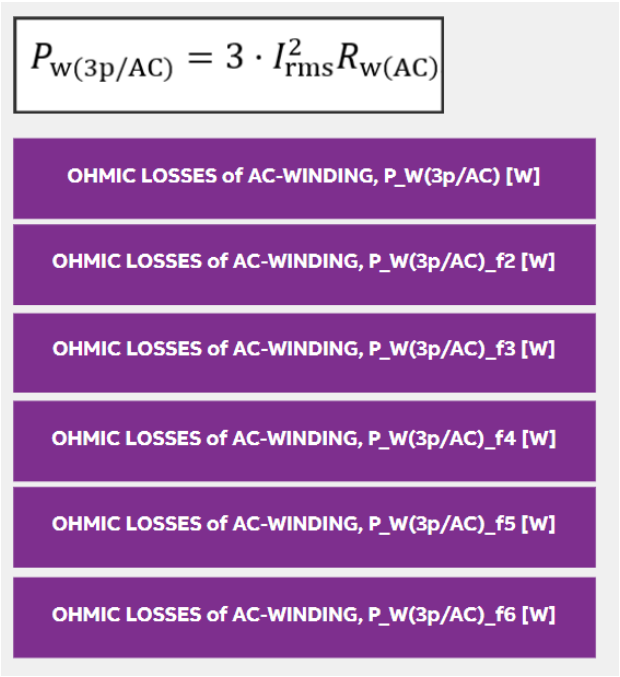

Figure 30. Determination of AC winding losses in six different frequency ranges.

5.2.2 Analytical loss calculation model for calculating AC winding losses using simulation software

This section examines the AC winding loss calculation tool, which can be found from Appendix 2. The loss calculation tool has been developed in the MATLAB environment. Figure 31 shows the winding losses of the choke prototype obtained using FEMM 2D simulation software. An ambient temperature of 20 °C was applied in all calculations. A foil-wound choke prototype with 13 winding turns was used in the simulations. Empty rows are available for choke prototypes with larger windings. Based on the initial results, winding losses increase near the core.

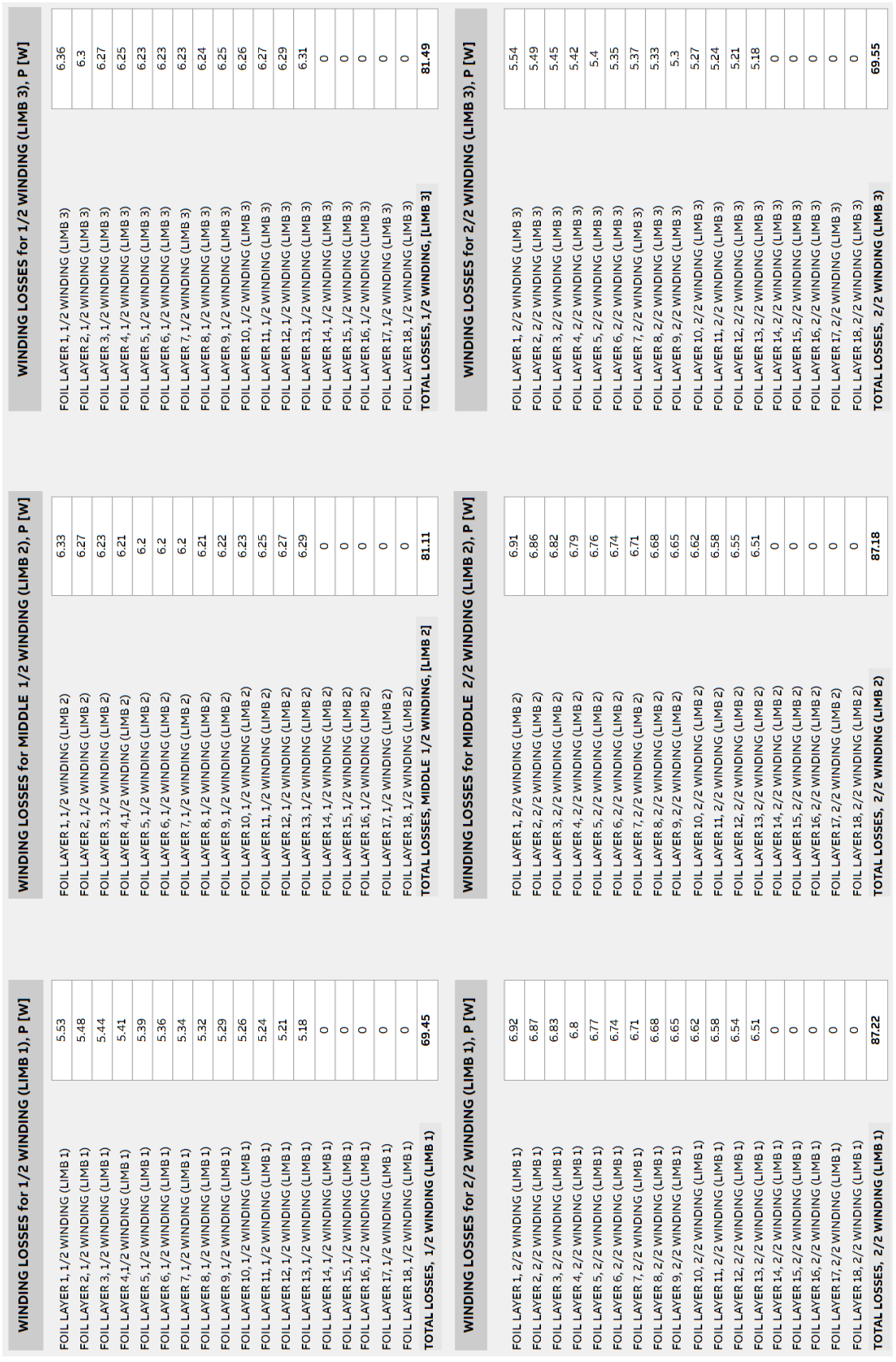

Figure 31. Simulated winding losses of the choke prototype.

Figure 32 examines the loss calculation in both 2D and 3D environments. 2D loss calculation has been implemented by utilizing existing geometric data and FEMM 2D simulation software. In addition to this, two separate 3D calculations have been developed, with a simplified and more accurate calculation. Simplified 3D calculation uses existing geometric data defined by segments. 3D design software has been applied in the accurate calculation. Geometrical data is defined in more detail in Appendix 2. The relative error is calculated from two results, indicating how well the results match each other.

LOSSES IN 2D, P [W]	
WINDING LOSSES, 1 - PHASE (2D)	156.7
WINDING LOSSES, 3 - PHASE (2D)	476

LOSSES IN 3D, P [W] (SIMPLIFIED)	
WINDING LOSSES, 1-PHASE (3D)	358.9
WINDING LOSSES, 3-PHASE (3D)	1090
WINDING LOSSES, 3-PHASE (SUPPLIER)	871
RELATIVE ERROR, % (SIMPLIFIED)	25.2

LOSSES IN 3D, P [W] (DETAILED)	
SEGMENT 1a	222.2
SEGMENT 1b	253.8
SEGMENT 3	270.5
SEGMENT 5	359.2
WINDING LOSSES, 1-PHASE (3D - DETAILED)	368.5
WINDING LOSSES, 3-PHASE (3D - DETAILED)	1106
WINDING LOSSES, 3-PHASE (SUPPLIER)	871
RELATIVE ERROR, % (DETAILED)	26.94

Figure 32. Definition of winding losses in 2D and 3D environment.

5.3 The results of calculation models and their comparison

This section examines the loss results of both calculation models. The calculations were obtained directly from the analytical calculation models and several choke prototypes were examined in the calculations. This thesis examines the calculations of one choke prototype and other prototypes are not discussed. The choke-based filter consists of three foil windings connected in parallel and the core is made of alloy steel. The foil winding is made of aluminum, the number of turns is 12.5 and the thickness is 1 mm. The number of air gaps per each column is 7 pieces. The breadth of the core cut sheet is 70 mm and the length of the laminated cut sheet pack is 110 mm. Liquid cooling works as the choke's cooling method. Losses are examined in Section 5.3.1 in the frequency range of 50 Hz to 18.2 kHz and rms in the range of 461 A to 0.5 A. In Section 5.3.2 in frequency 50 Hz and rms 461 A. Section 5.3.1 examines the results of the core and AC winding loss calculations of the analytical loss calculation model. The final version of the analytical tool can be found from Appendix 1. Section 5.3.2 examines the loss calculation results of the analytical AC winding loss calculation tool based on FEMM 2D, and the final version of the tool can be found from Appendix 2.

5.3.1 AC winding and core losses of the analytical calculation model

In this Section, using an analytical loss calculation tool, choke core losses and winding AC losses were determined in 6 frequency ranges using a numerical method based on MATLAB GUI. Six different calculations were made for the considered choke prototype in the frequency range of 50 Hz – 18.2 kHz. The calculation results of the core losses in relation to frequency are examined in more detail in Figure 33. Based on the results, at very low frequencies the losses are very small and correspondingly when going to 3.6 kHz frequencies the losses increase. The largest loss peak is at 3.6 kHz. However, losses do not increase linearly with frequency. When analyzing the losses at 7.3 kHz, it can be seen that the number of losses starts to decrease and continue to decrease at the highest frequencies. This can be explained by the fact that the losses depend on the material

used, which is therefore selected according to the application. Another factor is the structure of the core. Thus, the formation of hysteresis losses and eddy current losses at the highest frequencies is affected by the material used and the structure of the core.

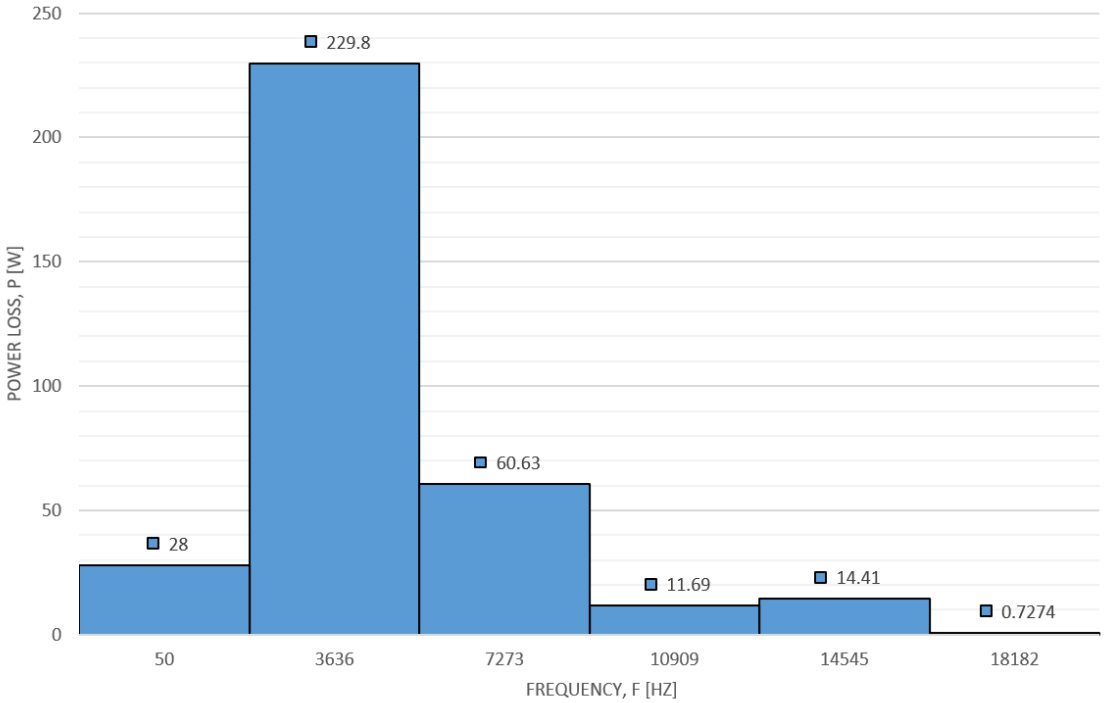

Figure 33. Core losses in 6 frequency ranges from 50 Hz to 18.2 kHz. Choke core losses were determined using an analytical loss calculation tool.

The winding losses of the choke prototype are examined in more detail in Figure 34. From the loss results of the bar charts, it can be concluded that winding losses are greatest at lower frequencies. This winding loss result is opposite when comparing it with the iron core loss result. This can be explained by the fact that skin and proximity effects are not taken into account in the calculation. Both phenomena affect at the highest frequencies. Since the choke prototype uses a foil conductor instead of a round conductor and the number of winding turns has been kept small, the number of losses is therefore reasonable. The windings have also been kept at a sufficient distance from the air gap in order to avoid overheating of the insulation at high frequencies and an increase in winding losses.

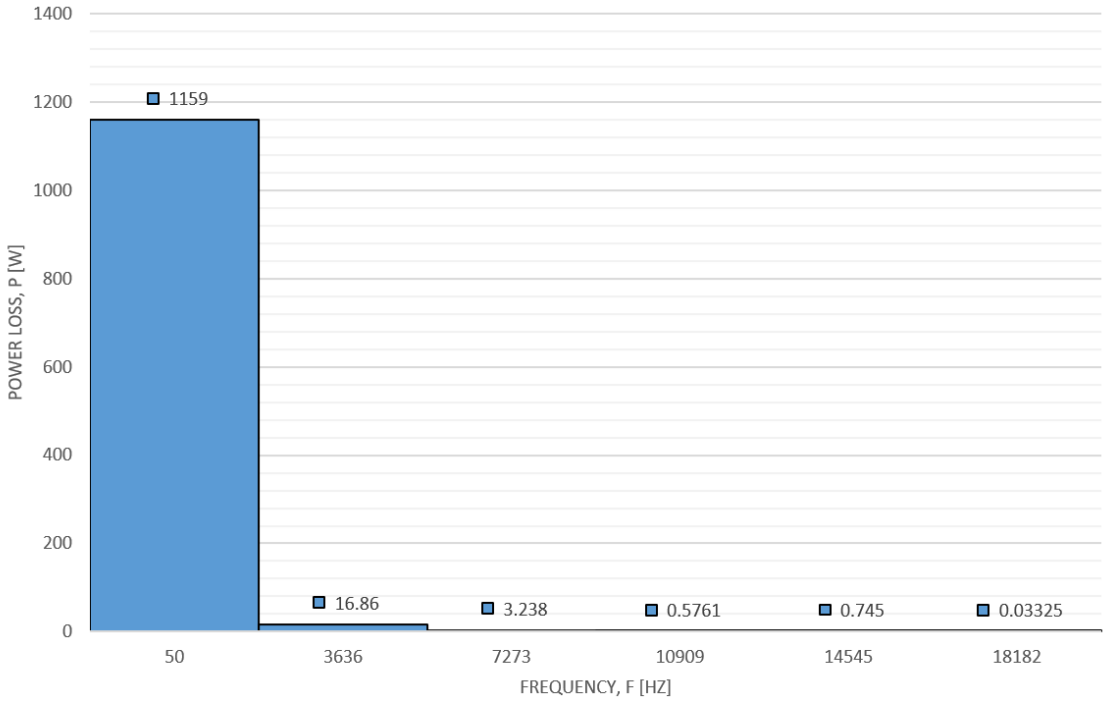

Figure 34. Winding losses in 6 frequency ranges from 50 Hz to 18.2 kHz. The AC winding losses of the choke-based filter were determined using an analytical loss calculation tool.

5.3.2 AC and DC winding losses of the analytical calculation model and their comparison with the simulation result

This Section examines the AC and DC winding losses of the choke-based filter using FEMM 2D simulation software. The results of the loss calculation tool have been obtained using analytical calculation tools designed into the MATLAB GUI environment. The AC winding losses of the choke prototype are examined in more detail in Figure 35. The bar chart compares the AC winding loss results of the two analytical calculation tools found in Appendices 1 and 2. The loss calculation results, illustrated by columns 1 – 3 in Figure 35, are obtained using the calculation tool found in Appendix 2. Similarly, the exact loss calculation result, illustrated by the column 4, is obtained by the analytical loss calculation tool found in Appendix 1. The left axis of the graph defines the losses of each column. The Comsol simulation software gives a loss calculation result of 871 W, and this result is compared with the results of the calculation tools found in Appendices 1 and 2.

This is illustrated by the orange curve, which gives relative error. Basically, the losses increase when moving from 2D calculation to 3D calculation. The loss calculation results of column 3 (calculation tool 2, Appendix 2) and column 4 (calculation tool 1, Appendix 1) correspond well to each other. When comparing the loss calculation result of column 3 with the simulated result, the relative error is 27 %. Similarly, when comparing the loss calculation result of column 4 with the simulated result, the relative error increases to 33 %. The difference between the analytical calculation model and the simulation result can be explained, for example, by the calculation of winding resistance, since precise calculation is possible only using defined equations.

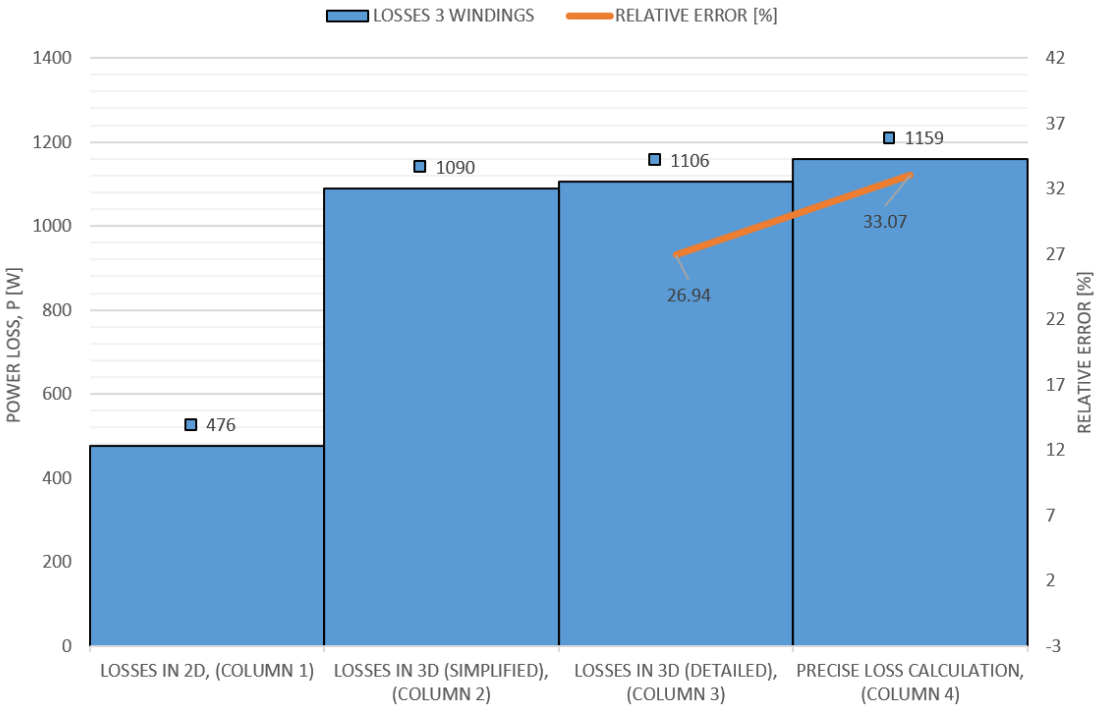

Figure 35. Columns illustrate the losses of an AC winding, where columns 1 to 3 are the loss calculation results of a 2D-3D environment (Appendix 2) and column 4 is the calculation result of a numerical method (Appendix 1). The relative error between the calculated losses and the simulation result is illustrated by the orange curve.

Figure 36 examines the DC winding losses. In this case the effects of skin and proximity effects do not need to be taken into account and the current is evenly distributed over the conductor's cross-section. The loss calculation result of the Comsol software is

694.3 W. As in the previous case, the winding losses increase if the winding geometry of the choke prototype is taken into account in the calculation. The relative error between the exact calculation and the simulation result is 13 %. From this it can be concluded that the results corresponded well to each other.

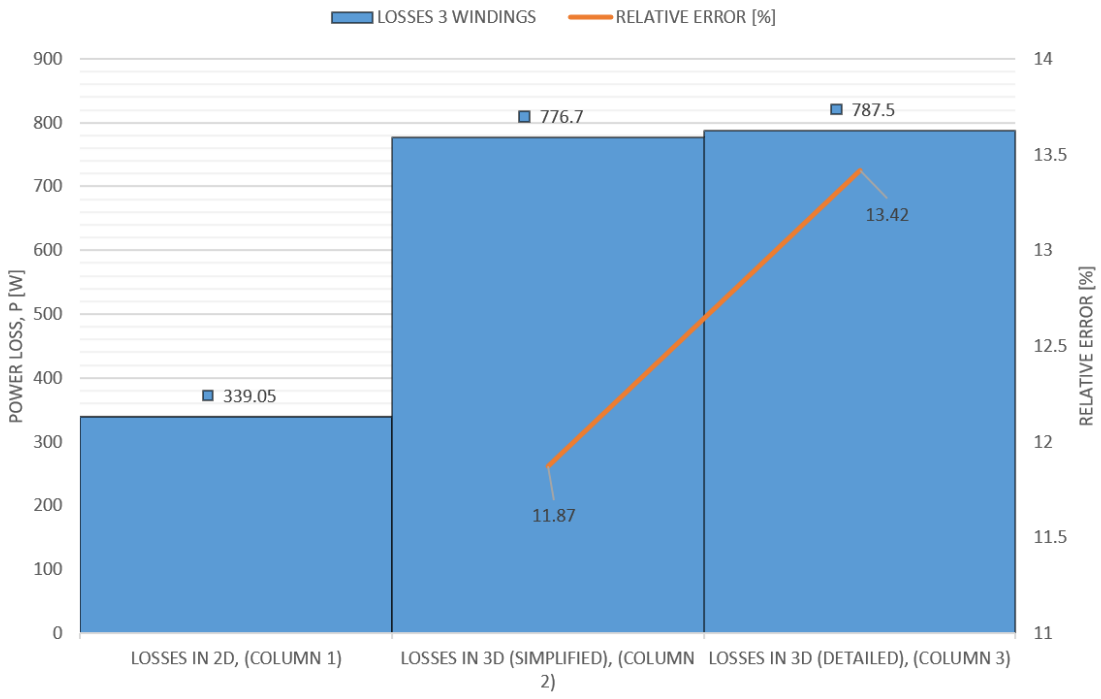

Figure 36. Columns illustrate DC winding losses, where columns 1-3 are the results of a 2D-3D environment loss calculation (Appendix 2). The margin of error between the calculated losses and the simulation result is illustrated by the orange curve.

6 Conclusion

This thesis studies the choke-based filter and its loss calculation. Power electronics-based devices, such as frequency converters and inverters, create harmonics and other unwanted effects on the power grid. Traditionally, the effect of harmonic currents and the quality of electricity have been improved using a choke-based filter. Depending on the level of interference currents, the interference currents strain the choke-based filter and limit its effectiveness. Interference currents increase the temperature of the filter, form eddy currents and cause additional losses.

The filter choke of the three-phase frequency converter cabinet consists of three windings connected in parallel and a core. A foil conductor is used as a winding conductor instead of a round conductor to reduce the size, weight and losses of the component. The thin and large cross-sectional area of the foil winding conductor decreases the value of resistance, as well as provides better heat dissipation and cooling. Typically, a core is made by assembling a core from cut sheets. To reduce eddy current losses, the cut sheets are insulated from each other by lamination.

The core losses of the choke consist mainly of hysteresis and eddy current losses, and the winding losses consist of eddy current losses. Hysteresis losses are caused by the fact that when magnetizing the core, energy is needed to change its magnetic state. The required energy, which is examined from the *BH* characteristic curve, is directly proportional to the area of the hysteresis loop. The increase in the area of the hysteresis loop is affected by the material, temperature, size and frequency of the core. Eddy current losses are formed when alternating current is fed into the conductor, which generates a time-varying magnetic field strength around the conductor. The time-varying magnetic field generates eddy currents, which form losses in the conducting core. Eddy currents depend on the conductivity and geometry of the core. The direct current in the winding causes losses in the winding due to its resistance. When going to 100 kHz frequencies, the current is no longer evenly distributed over the cross-section of the conductor due

to the skin and proximity effects. In this thesis, losses are examined in the frequency range of 50 Hz – 18.2 kHz and skin and proximity effects are not taken into account.

The purpose of this study was to examine the loss calculation of a foil winding choke and to develop analytical calculation models to support the design of the main circuit. The analytical calculation models were designed to be easy to use, accurate, reliable, and flexible. Calculation models should calculate the winding and core losses of the choke. Calculation tools must be able to determine the choke losses at different loading points when output frequency and modulation index vary. The literature review provides a theoretical background on AC-AC and DC-AC converters, winding and core structure, magnetic materials, and filter topologies. In addition, the literature review discusses the resulting core and winding losses and their calculation.

After the literature review one filter prototype is selected for simulations and analytical calculation models. The choke-based filter prototype for which the necessary loss calculations were performed, consists of three foil windings connected in parallel, and the core material was alloy steel. The simulations were performed using the FEMM 2D software. Simulations were needed to verify the accuracy of the calculation tools.

As a result of the work, the necessary numerical calculation tools were designed, both of which were developed for the MATLAB programming environment. The operation of the calculation models was confirmed by simulations. For DC winding losses, the analytical calculation model and simulation result had a relative error of 13 %, indicating that the results corresponded well to each other. Similarly, for AC winding losses, the relative error of the analytical calculation model and the simulation result was 27 %. This difference can be explained by the incomplete simulation result of the simulation software. Core losses were modeled using the Steinmetz equation. According to the analytical calculation model, the greatest losses in the frequency range from 50 Hz to 18.2 kHz occurred at 3.6 kHz. Analytical calculation tools showed promising calculation results. In any case, the calculation models require further research and expansion to determine a

more accurate loss calculation. However, the developed calculation models serve as a basis for determining the winding and core losses. Further research is needed to include the required characteristics of choke prototypes in the loss calculation, such as core and winding materials, weight, maximum allowable temperature, skin and proximity effects. The core material of the different choke prototypes must be selected based on simulations and a more accurate calculation model. The new core loss calculation model i^2GSE may be considered here (Muhlethaler & others, 2011, p. 964). In addition, winding losses and transient behavior of the choke prototype should be studied in a 3D environment. An Ansys 3D design tool or Comsol Multiphysics simulation software may be considered here.

References

Albach, M. (2011). *Elektrotechnik* (1st edition). Pearson Studium.

Albach, M. (2017). *Induktivitäten in der Leistungselektronik*. Springer Vieweg Wiesbaden. https://doi.org/10.1007/978-3-658-15081-5

Albach, M., & Fischer, J. (2020). *Elektrotechnik Aufgabensammlung* (2nd edition). Pearson Deutschland GmbH

Biela, J. (2005). *Optimierung des elektromagnetisch integrierten serien-parallel-resonanzkonverters mit eingeprägtem ausgangsstrom* [Doctoral dissertation, ETH Zurich]. ETH Zurich. https://doi.org/10.3929/ethz-a-005582936

Biela, J. (2011, 17. March). *Wirbelstromverluste in Wicklungen induktiver Bauelemente* [Educational material]. ETH Zurich, Laboratory for High Power Electronic Systems. https://doi.org/10.3929/ethz-b-000604056

Biela, J., Gfrörer, T., & Jeong, M. (2022, 23. June). *Extending Stable Parameter Range of LCL- filters for Grid-Connected Converters by Inherent Damping of Model Predictive Control* (MPC) [White paper]. 2022 IEEE 23rd Workshop on Control and Modeling for Power Electronics (COMPEL), 1–8. https://doi.org/10.1109/compel53829.2022.9829978

Bußmann, B., K. (2014). *Untersuchung von leitfähigen Schichtsystemen mittels Rasterkraftmikroskopie* [Doctoral dissertation, University of Duisburg-Essen]. Duisburg-Essen University Library. Retrieved 23.01.2023 from https://core.ac.uk/download/pdf/33797192.pdf

Chemie. (2022). Lexikon: *spezifischer widerstand.* Retrieved 04.01.2023 from https://www.chemie.de/lexikon/Spezifischer_Widerstand.html

Cheever, E. (n.d.). *The Asymptotic Bode Diagram: Derivation of Approximations*. Linear Physical System Analysis. Retrieved 15.04.2023 from https://lpsa.swarthmore.edu/Bode/BodeHow.html

Coey, J. M. D. (2010). *Magnetism and Magnetic Materials*. Cambridge University Press.

Dadafshar, M. (2012). *Designing high frequency planar transformers*. Pulse Electronics. Retrieved 04.01.2023 from https://www.tti.com/content/dam/ttiinc/manufacturers/pulse/PDF/Pulse-Power-BU-Designing-High-Frequency-Planar-Transformers.pdf

Dauhajre, A., & Middlebrook, R. D. (1986, 23-27. June). *Modelling and estimation of leakage phenomena in magnetic circuits*. 17th Annual IEEE Power Electronics Specialists Conference, 213–226. https://doi.org/10.1109/PESC.1986.7415565

Dowell, P. L. (1966, 8. August). *Effects of eddy currents in transformer windings* [White paper]. IEEE, 113(8), 1387–1394. Retrieved 02.01.2023 from http://www.cpdee.ufmg.br/~troliveira/docs/aulas/fontes/05247417.pdf

Emetor. (2030). *Stacking factor*. Retrieved 04.01.2023 from https://www.emetor.com/glossary/stacking-factor/

Erickson, R. W., & Maksimovic, M. (2020). *Fundamentals of Power Electronics* (3rd edition). Springer Cham. https://doi.org/10.1007/978-3-030-43881-4

European passive components institute. (2023). *Ripple Current and its Effects on the Performance of Capacitors*. EPCI-Premium Passive Components Educational and Informational. Retrieved 11.04.2023 from https://passive-components.eu/ripple-current-and-its-effects-on-the-performance-of-capacitors/

Freitag, C. (2017, 9. February). *Magnetic properties of electrical steel, power transformer core losses and core design concepts* [Doctoral dissertation, Karlsruher Institut fur Technologie]. Repository KITopen. https://doi.org/10.5445/IR/1000066142

Grahn, P. (2022). *Special Topics in Field Theory*, SATE2270-3001 [Educational material]. *Moodle.* Retrieved 6.11.2022 from https://moodle.uwasa.fi/course/view.php?id=7502

Haanpää, K. (2016). *LCL-suodattimella varustetun verkkosuuntaajan virtasäätö tilasäädintä ja -havaitsijaa käyttäen* [Master's thesis, Aalto University]. Aaltodoc. http://urn.fi/URN:NBN:fi:aalto-201604201811

Hayt, W., H., & Buck, J., A. (2012). *Engineering electromagnetics* (8th edition). McGraw-Hill Companies. Retrieved 19.02.2023 from http://www.uop.edu.pk/ocontents/EMT.pdf

Heinz Schmidt-Water. (n.d.). *Choking Coil*: *Calculation of choking-coils and flyback transformers*. Retrieved 04.01.2023 from http://schmidt-walter-schaltnetzteile.de/smps_e/etd_hilfe_e.html

Hurley, W. G., & Wölfe, W. H. (2013). *Transformers and inductors for power electronics: theory, design and applications*. John Wiley & Sons, Ltd. https://doi.org/10.1002/9781118544648

IEEE Standard for Harmonic Control in Electric Power Systems. (2022). *519-2022 - IEEE Standard for Harmonic Control in Electric Power Systems* (Revision of IEEE Std 519–2014). https://doi.org/10.1109/IEEESTD.2022.9848440

International Electrotechnical Commission. (2021). Adjustable speed electrical power drive systems - Part 9-2: Ecodesign for motor systems-Energy efficiency determination and classification (IEC 61800-9-2 ED2).

Karshenas, H., & Saghafi, H. (2006, 12. July). *Basic Criteria in Designing LCL Filters for Grid Connected Converters*. 2006 IEEE International Symposium on Industrial Electronics, 1996–2000. https://doi.org/10.1109/ISIE.2006.295879

Kartsonakis, V. (2021). *Semiconductors Power Losses in a Three-phase Inverter using MATLAB Application Designer* [Master's thesis, Aalborg University]. Aalborg Universitet project library. Retrieved 26.01.2023 from https://projekter.aau.dk/projekter/files/414361234/PED4_1042_Report.pdf

Kazimierczuk, M. K. (2014). *High-frequency magnetic component*. John Wiley and Sons, Ltd. https://doi.org/10.1002/9781118717806.ch6

Kesarkar, A., and Narayanasamy (2019, July). *Asymptotic magnitude Bode plots of fractional-order transfer functions* [White paper]. IEEE/CAA Journal of Automatica Sinica, 6(4), 1019–1026. https://doi.org/10.1109/JAS.2016.7510196

Kolar, J. W. J., Schäfer, J. & Bortis, D. (2018). *Optimal Design of Highly Efficient and Highly Compact PCB Winding Inductors* [White paper]. 2018 IEEE 19th Workshop on Control and Modeling for Power Electronics (COMPEL). https://doi.org/10.1109/COMPEL.2018.8460166

Koskinen, H. (2016). *Elektrodynamiikka*. University of Helsinki. Retrieved 5.5.2023 from http://www.courses.physics.helsinki.fi/teor/ed/Moniste_2016/ED2016.pdf

Krall, F. (2017). *Analysis and Implementation of Algorithms for Calculation of Iron Losses for Fractional Horsepower Electric Motors* [Master's thesis, Master's Thesis, Graz

University of Technology (90000)]. TUGraz DIGITAL Library. Retrieved 5.5.2023 from https://diglib.tugraz.at/download.php?id=5aa247c5dc8bd&location=browse

Kumari, D. (2014). *Optimal LCL filter design for grid-interfaced distributed power generation system* [Master's thesis, National Institute Technology, Rourkela]. NIT Rourkela. Retrieved 16.03.2023 from https://core.ac.uk/download/pdf/80147104.pdf

Lehto, E. (2012). *Taajuusmuuttajan välipiirikiskojen suunnittelu: Laminoidut kiskot ja induktanssin pienentämien* [Master's thesis, University of Vaasa]. Osuva. http://osuva.uwasa.fi/handle/10024/2559

Loncarski, J. (2014, 24. June). *Analysis of the Current Ripple in Three-Phase Two-Level VSIs*. Springer International Publishing, Cham, 5–31. https://doi.org/10.1007/978-3-319-07251-7_2

Malinen, E. (2017). *Practical approach to main circuit and EMI filter design of a 15 kW dual active bridge converter* [Master's thesis, Lappeenranta University of Technology]. LUTPub. https://urn.fi/URN:NBN:fi-fe2017110250474

McLyman, C. W. T. (2004). *Transformer and inductor design handbook* [3rd edition]. CRC Press. https://doi.org/10.1201/9780203913598

Meyer, R., & Martens, A. (2012, 20. Septemper). *Design of LCL filters in consideration of parameter variations for grid-connected converters*. 2012 IEEE Energy Conversion Congress and Exposition (ECCE), 557–564. https://doi.org/10.1109/ECCE.2012.6342772

Muhlethaler, J., Biela, J., Kolar, J. W., & Ecklebe, A. (2011, 18. July). *Improved Core-Loss Calculation for Magnetic Components Employed in Power Electronic Systems* [White paper]. IEEE Transactions on Power Electronics, 27(2), 964–973. https://doi.org/10.1109/TPEL.2011.2162252

Muhlethaler, J. (2012). *Modeling and multi-objective optimization of inductive power components* [Doctoral dissertation, Swiss Federal Institute of Technology in Zürich]. ETH Zurich. https://doi.org/10.3929/ethz-a-007328104

Multon, P., Deu, J. F., Aucejo, M., & Lossouarn, B. (2017, March 28). Design of inductors with high inductance values for resonant piezoelectric damping. Sensors and Actuators A: Physical, 259(1), 68–76. https://doi.org/10.1016/j.sna.2017.03.030

Oikonomou, C. (2014). *Surface Characterization of Soft Magnetic Composite Powder and Compacts* [Doctoral dissertation, Chalmers University of Technology]. Chalmers Publication Library. Retrieves 24.3.2023 from https://core.ac.uk/download/pdf/70606267.pdf

Paakkinen, M. (2014). *Limittelymenetelmän hyödyntäminen verkkovaihtosuuntaajassa: LCL-suotimen mitoitus* [Master's thesis, Lappeenranta-Lahti University of Technology LUT]. LUTPub. https://urn.fi/URN:NBN:fi-fe2014051525868

Park, K-P., Kieferndorf, F., Drofenik, U., Petterson, S., & Canales, F. (2015, 5. June). *Weight minimization of LCL filters for high power converters*. 2015 9th International Conference on Power Electronics and ECCE Asia (ICPE-ECCE Asia), 142–149. https://doi.org/10.1109/ICPE.2015.7167778

Prsa, M. A., Kasaš-Lažetić, K. K., & Mucalica, N. D. (2011, 23. June). *Skin effect and proximity effect in a real, high voltage, double three-phase system* [White paper].

2011 IEEE EUROCON - International Conference on Computer as a Tool. https://doi.org/10.1109/EUROCON.2011.5929245

Rahman, F. M. M. (2016). *Converter-side inductor design for a grid-connected converter equipped with an LCL filter* [Master's thesis, Aalto University]. Aaltodoc. http://urn.fi/URN:NBN:fi:aalto-201604201826

Raina, K. B., & Bhattacharya A. K. (1991). *Electrical design estimating and coasting*. New Age International (P) Ltd.

Rantanen, A. (2017). *Design of a low loss and cost-efficient choke for a general purpose frequency converter* [Master's thesis, Tampere University]. Trepo. https://urn.fi/URN:NBN:fi:tty-201709251957

Rhuan, X., Wang, X., Pan, D., Yang, D., Li, W., & Bao, C. (2018). *Control Techniques for LCL-Type Grid-Connected Inverters*. Springer Singapore. https://doi.org/10.1007/978-981-10-4277-5

Romirer, R. (2012). *Temperaturabhängige widerstandsmessung mit der vierpunktmethode* [Master's thesis, Graz University of Technology]. TUGraz DIGITAL Library. Retrieved 08.01.2023 from https://diglib.tugraz.at/download.php?id=576a76710046d&location=browse

Sadiku, M. (2018). *Elements of Electromagnetics* (7th edition). Oxford University Press.

Saket, A. (2020, 26. February). *High-Frequency Magnetic Design*. The University of British Columbia, Electrical & Computer Engineering. Retrieved 18.02.2023 from https://people.ece.ubc.ca/alisaket/Analytic_Design_and_FEA_Modeling_of_Magnetic.html

Sobolewski, J. S. (2004). *Data Transmission Media*. Encyclopedia of Physical Science and Technology (Third edition), 277–303. https://doi.org/10.1016/B0-12-227410-5/00165-4

Stenglein, E. (2021, 06. May). *Messtechnische Charakterisierung und Vorhersage der Kernverluste bei weichmagnetischen Ferriten* [Doctoral dissertation, Friedrich-Alexander-Universität Erlangen-Nurnberg]. Friedrich-Alexander-Universität Erlangen-Nurnberg. https://nbn-resolving.org/urn:nbn:de:bvb:29-opus4-165283

Tarter, R. E. (1993). *Solid-State Power Conversion Handbook* (1st edition). Wiley-Interscience.

Transfer Multisort Elektronik. (2020). *Mikä on induktiokela ja mihin sitä käytetään elektroniikassa*. Retrieved 15.03.2023 from https://www.tme.eu/fi/news/library-articles/page/42527/mika-on-induktiokela-ja-mihin-sita-kaytetaan-elektroniikassa/

Wang, T. C. Y., Ye, Z, Sinha, G. & Yuan, X. (2003). *Elektrotechnik Aufgabensammlung* [White paper]. IEEE 34th Annual Conference on Power Electronics Specialist, 2003, PESC ´03, p. 779–784. https://doi.org/10.1109/PESC.2003.1218154

Yagnit, U. P., & Solanki, M. D. (2017, 12. May). *Comparison of L, LC & LCL filter for grid connected converter* [White paper]. 2017 International Conference on Trends in Electronics and Informatics (ICEI). https://doi.org/10.1109/ICOEI.2017.8300968

Zach, F. (2015). *Leistungselektronik* (1st and 2nd edition). Springer Vieweg Wiesbaden. https://doi.org/10.1007/978-3-658-04899-0

Zaitseva, K. (2012). *Aurinkosähköjärjestelmien, elektronisesti kommutoitujen tasavirtamoottoreiden ja LED-valaistuksen käytön vaikutus rakennusten sähkön laatuun*

[Master's thesis, Aalto University]. Aaltodoc. http://urn.fi/URN:NBN:fi:aalto-201209213114

Zare, F., Soltani, H., Kumar, D., Davari, P., Delpino, H. A. M., & Blaabjerg, F. (2017, 16. February). *Harmonic Emissions of Three-Phase Diode Rectifiers in Distribution Networks* [White paper]. IEEE Access, 5, 2819 – 2833. https://doi.org/10.1109/ACCESS.2017.2669578

Zulk, S. (2021). *Optimierung eines einphasigen PFC-Gleichrichters mit Wide-Bandgap-Leistungshalbleitern auf Basis domänenübergreifender Modelle* [Doctoral dissertation, Gottfried Wilhelm Leibniz University Hannover]. Leibniz Universität Hannover Institutional Repository. https://doi.org/10.15488/10513

Appendices

Appendix 1. Analytical calculation model for core and winding losses

This appendix describes an analytical loss calculation model for determining core and winding losses. The calculation model is analyzed in more detail in Section 5.2.1. The loss calculation model was designed for the MATLAB environment by utilizing the equations discussed in the theory part. The application works in such a way that the numerical calculation defined in the MATLAB programming environment calculates the important core and winding losses using the relevant equations. The most important variables, such as the frequency range and the rms value of the current can be modified directly from the pop-up window of the calculation model. Losses are defined in six different frequency ranges from 50 Hz to 18.2 kilohertz (kHz). The user interface of this tool is shown in Figure.

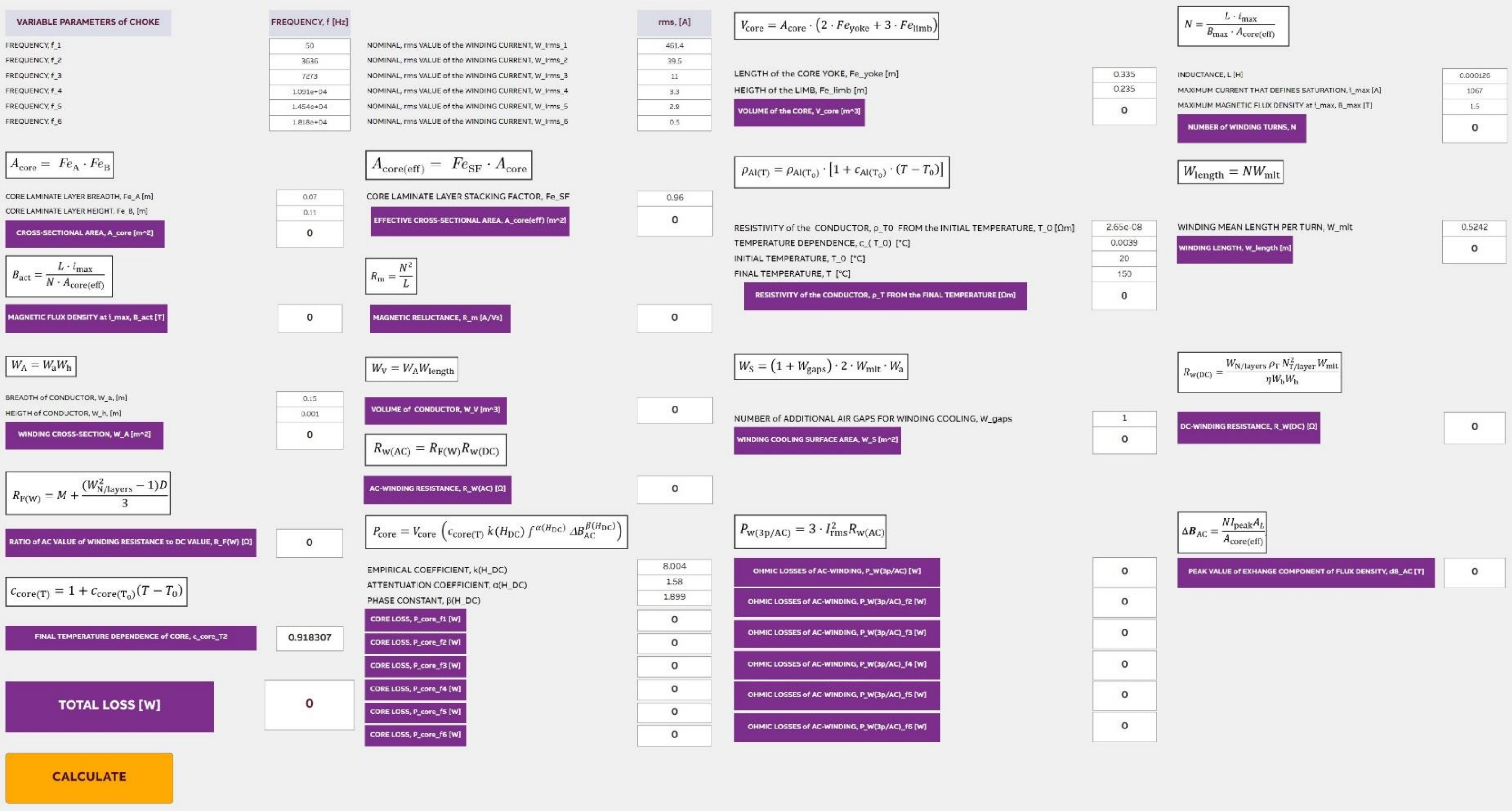

VARIABLE PARAMETERS of CHOKE	FREQUENCY, f [Hz]		rms, [A]
FREQUENCY, f_1	50	NOMINAL, rms VALUE of the WINDING CURRENT, W_Irms_1	461.4
FREQUENCY, f_2	3636	NOMINAL, rms VALUE of the WINDING CURRENT, W_Irms_2	39.5
FREQUENCY, f_3	7273	NOMINAL, rms VALUE of the WINDING CURRENT, W_Irms_3	11
FREQUENCY, f_4	1.091e+04	NOMINAL, rms VALUE of the WINDING CURRENT, W_Irms_4	3.3
FREQUENCY, f_5	1.454e+04	NOMINAL, rms VALUE of the WINDING CURRENT, W_Irms_5	2.9
FREQUENCY, f_6	1.818e+04	NOMINAL, rms VALUE of the WINDING CURRENT, W_Irms_6	0.5

$$A_{\text{core}} = Fe_{\text{A}} \cdot Fe_{\text{B}}$$

CORE LAMINATE LAYER BREADTH, Fe_A [m] 0.07
CORE LAMINATE LAYER HEIGHT, Fe_B, [m] 0.11
CROSS-SECTIONAL AREA, A_core [m^2] 0

$$B_{\text{act}} = \frac{L \cdot i_{\max}}{N \cdot A_{\text{core(eff)}}}$$

MAGNETIC FLUX DENSITY at i_max, B_act [T] 0

$$W_{\text{A}} = W_{\text{a}} W_{\text{h}}$$

BREADTH of CONDUCTOR, W_a, [m] 0.15
HEIGTH of CONDUCTOR, W_h, [m] 0.001
WINDING CROSS-SECTION, W_A [m^2] 0

$$R_{\text{F(W)}} = M + \frac{(W_{\text{N/layers}}^2 - 1)D}{3}$$

RATIO of AC VALUE of WINDING RESISTANCE to DC VALUE, R_F(W) [Ω] 0

$$c_{\text{core(T)}} = 1 + c_{\text{core}(\text{T}_0)}(T - T_0)$$

FINAL TEMPERATURE DEPENDENCE of CORE, c_core_T2 0.918307

TOTAL LOSS [W] 0

CALCULATE

$$A_{\text{core(eff)}} = Fe_{\text{SF}} \cdot A_{\text{core}}$$

CORE LAMINATE LAYER STACKING FACTOR, Fe_SF 0.96
EFFECTIVE CROSS-SECTIONAL AREA, A_core(eff) [m^2] 0

$$R_{\text{m}} = \frac{N^2}{L}$$

MAGNETIC RELUCTANCE, R_m [A/Vs] 0

$$W_{\text{V}} = W_{\text{A}} W_{\text{length}}$$

VOLUME of CONDUCTOR, W_V [m^3] 0

$$R_{\text{w(AC)}} = R_{\text{F(W)}} R_{\text{w(DC)}}$$

AC-WINDING RESISTANCE, R_W(AC) [Ω] 0

$$P_{\text{core}} = V_{\text{core}} \left(c_{\text{core(T)}}\, k(H_{\text{DC}})\, f^{\alpha(H_{\text{DC}})}\, \Delta B_{\text{AC}}^{\beta(H_{\text{DC}})} \right)$$

EMPIRICAL COEFFICIENT, k(H_DC) 8.004
ATTENTUATION COEFFICIENT, α(H_DC) 1.58
PHASE CONSTANT, β(H_DC) 1.899
CORE LOSS, P_core_f1 [W] 0
CORE LOSS, P_core_f2 [W] 0
CORE LOSS, P_core_f3 [W] 0
CORE LOSS, P_core_f4 [W] 0
CORE LOSS, P_core_f5 [W] 0
CORE LOSS, P_core_f6 [W] 0

$$V_{\text{core}} = A_{\text{core}} \cdot \left(2 \cdot Fe_{\text{yoke}} + 3 \cdot Fe_{\text{limb}}\right)$$

LENGTH of the CORE YOKE, Fe_yoke [m] 0.335
HEIGTH of the LIMB, Fe_limb [m] 0.235
VOLUME of the CORE, V_core [m^3] 0

$$\rho_{\text{Al(T)}} = \rho_{\text{Al}(\text{T}_0)} \cdot \left[1 + c_{\text{Al}(\text{T}_0)} \cdot (T - T_0)\right]$$

RESISTIVITY of the CONDUCTOR, ρ_T0 FROM the INITIAL TEMPERATURE, T_0 [Ωm] 2.65e-08
TEMPERATURE DEPENDENCE, c_(T_0) [°C] 0.0039
INITIAL TEMPERATURE, T_0 [°C] 20
FINAL TEMPERATURE, T [°C] 150
RESISTIVITY of the CONDUCTOR, ρ_T FROM the FINAL TEMPERATURE [Ωm] 0

$$W_{\text{S}} = \left(1 + W_{\text{gaps}}\right) \cdot 2 \cdot W_{\text{mlt}} \cdot W_{\text{a}}$$

NUMBER of ADDITIONAL AIR GAPS FOR WINDING COOLING, W_gaps 1
WINDING COOLING SURFACE AREA, W_S [m^2] 0

$$P_{\text{w(3p/AC)}} = 3 \cdot I_{\text{rms}}^2 R_{\text{w(AC)}}$$

OHMIC LOSSES of AC-WINDING, P_W(3p/AC) [W] 0
OHMIC LOSSES of AC-WINDING, P_W(3p/AC)_f2 [W] 0
OHMIC LOSSES of AC-WINDING, P_W(3p/AC)_f3 [W] 0
OHMIC LOSSES of AC-WINDING, P_W(3p/AC)_f4 [W] 0
OHMIC LOSSES of AC-WINDING, P_W(3p/AC)_f5 [W] 0
OHMIC LOSSES of AC-WINDING, P_W(3p/AC)_f6 [W] 0

$$N = \frac{L \cdot i_{\max}}{B_{\max} \cdot A_{\text{core(eff)}}}$$

INDUCTANCE, L [H] 0.000126
MAXIMUM CURRENT THAT DEFINES SATURATION, i_max [A] 1067
MAXIMUM MAGNETIC FLUX DENSITY at i_max, B_max [T] 1.5
NUMBER of WINDING TURNS, N 0

$$W_{\text{length}} = N W_{\text{mlt}}$$

WINDING MEAN LENGTH PER TURN, W_mlt 0.5242
WINDING LENGTH, W_length [m] 0

$$R_{\text{w(DC)}} = \frac{W_{\text{N/layers}}\, \rho_{\text{T}}\, N_{\text{T/layer}}^2\, W_{\text{mlt}}}{\eta W_{\text{b}} W_{\text{h}}}$$

DC-WINDING RESISTANCE, R_W(DC) [Ω] 0

$$\Delta \boldsymbol{B}_{\text{AC}} = \frac{N I_{\text{peak}} A_L}{A_{\text{core(eff)}}}$$

PEAK VALUE of EXHANGE COMPONENT of FLUX DENSITY, dB_AC [T] 0

Figure 37. Analytical loss calculation model of the choke-based filter for calculating core and AC winding losses.

Appendix 2. Analytical calculation model for AC winding losses

This appendix describes the AC winding loss calculation tool, which is further analyzed in Section 5.2.2. The loss calculation tool was designed for the MATLAB environment. The simulation software was needed, among other things, to determine the choke geometry and winding losses in a 2D environment, which were applied to the calculation model. In addition, the simulation software provided valuable information to refine the calculation. The loss calculation results of two 3D calculation modeling (simplified and detailed) are compared with the simulated loss calculation result, which gives a relative error. The relative error gives an indication of how well the results match each other. Simplified 3D calculation uses existing geometric data defined by segments. 3D design software has been used in the precise calculation. The user interface of this tool is shown in Figure.

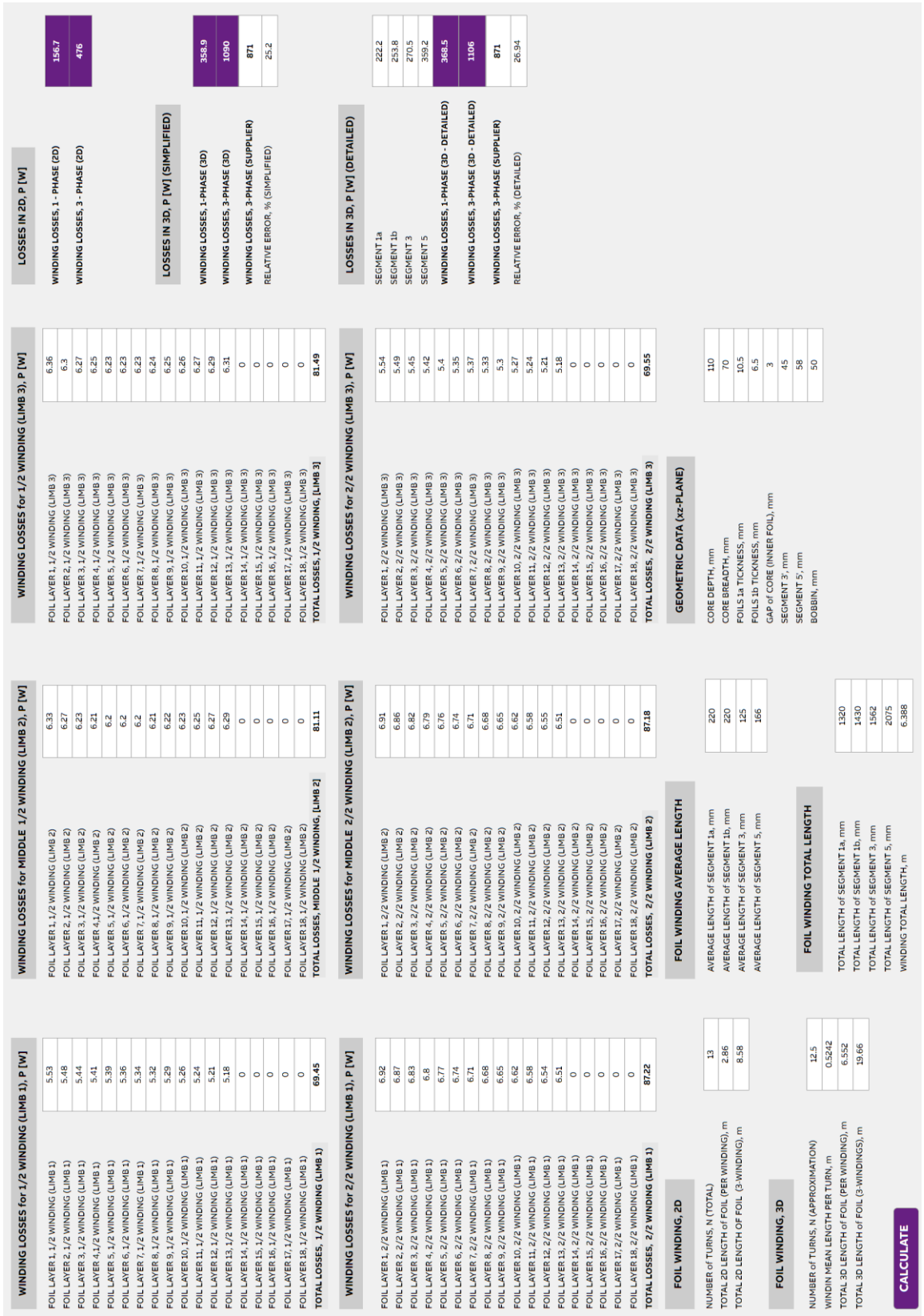

Figure 38. Analytical loss calculation model of the choke-based filter for calculating AC winding losses. The calculation model uses the FEMM 2D simulation software.